National Library
of Canada

Bibliothèque nationale
du Canada

Acquisitions and
Bibliographic Services Branch

Direction des acquisitions et
des services bibliographiques

395 Wellington Street
Ottawa, Ontario
K1A 0N4

395, rue Wellington
Ottawa (Ontario)
K1A 0N4

Your file Votre référence

Our file Notre référence

NOTICE

The quality of this microform is heavily dependent upon the quality of the original thesis submitted for microfilming. Every effort has been made to ensure the highest quality of reproduction possible.

If pages are missing, contact the university which granted the degree.

Some pages may have indistinct print especially if the original pages were typed with a poor typewriter ribbon or if the university sent us an inferior photocopy.

Reproduction in full or in part of this microform is governed by the Canadian Copyright Act, R.S.C. 1970, c. C-30, and subsequent amendments.

AVIS

La qualité de cette microforme dépend grandement de la qualité de la thèse soumise au microfilmage. Nous avons tout fait pour assurer une qualité supérieure de reproduction.

S'il manque des pages, veuillez communiquer avec l'université qui a conféré le grade.

La qualité d'impression de certaines pages peut laisser à désirer, surtout si les pages originales ont été dactylographiées à l'aide d'un ruban usé ou si l'université nous a fait parvenir une photocopie de qualité inférieure.

La reproduction, même partielle, de cette microforme est soumise à la Loi canadienne sur le droit d'auteur, SRC 1970, c. C-30, et ses amendements subséquents.

Canada

Design, Control and Energy Minimization Strategies for an Electrically Actuated Legged Robot

Pedro Gregorio

Department of Mechanical Engineering
McGill University, Montreal

January 1995

A Thesis submitted to the Faculty of Graduate Studies and Research in partial fulfillment of the requirements of the degree of Master of Engineering

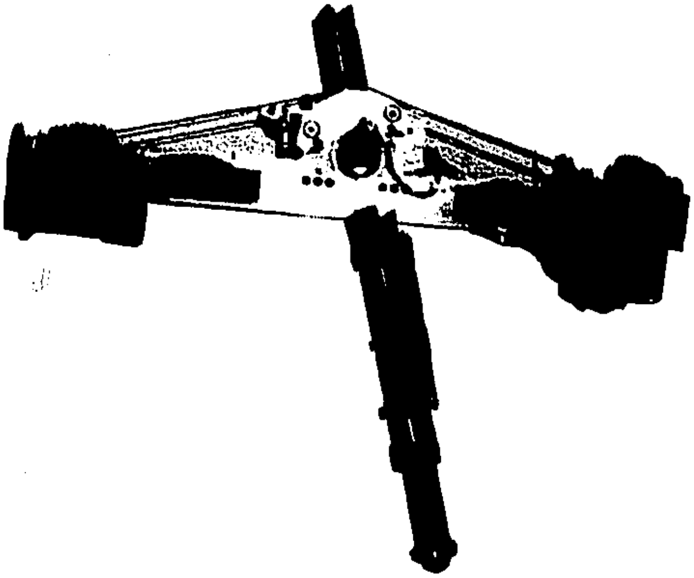

National Library
of Canada

Acquisitions and
Bibliographic Services Branch

395 Wellington Street
Ottawa, Ontario
K1A 0N4

Bibliothèque nationale
du Canada

Direction des acquisitions et
des services bibliographiques

395, rue Wellington
Ottawa (Ontario)
K1A 0N4

Your file Votre référence

Our file Notre référence

ISBN 0-612-05450-0

Canada

The title may be shortened for the spine as follows:

Design, Control and Energy Minimization Strategies for a Legged Robot

To my father

Abstract

We have built a planar one-legged robot (the ARL Monopod) to study the design, control and energetics of autonomous dynamically stable legged machines. Our $15kg$ robot is actuated by two low power $80W$ DC electric motors, yet it operates in a stable and robust fashion up to a running speed of $4.3km/hr$ ($1.2m/s$). Both design and control of our machine borrow heavily from Raibert's work whose robots use much more powerful hydraulic actuators. Despite our comparatively low power available for actuation, only the hopping height controller had to be modified to achieve stable running. In order to improve energetic efficiency we introduced a scalar "locomotion time" variable, which maps one locomotion cycle onto a fixed interval, independent of operating conditions. This locomotion time has allowed the implementation of a reference trajectory for flight phase leg angle tracking. We have performed a detailed energetic analysis of robot running for the ARL monopod in order to determine how its efficiency may be improved. A comparative energetic analysis reveals our machine as the most energy efficient powered legged robot having a specific resistance of $\varepsilon = 0.7$ at $4.3km/hr$ ($1.2m/s$) running speed.

Résumé

On a construit on robot marcheur a une patte (le Monopod ARL) pour étudier le design, le contrôle et la performance énergétique des robots marcheurs autonomes et dynamiquement stables. Notre robot de 15kg est activé par deux moteurs électriques à courant continu de faible puissance (80W). Malgré cela, il se déplace d'une manière stable et robuste et atteint une vitesse de pointe de $4.3km/hr$ $(1.2m/s)$. *Le design et le contrôle de base sont empruntés des travaux de Raibert où les robots sont activés par des actionneurs hydrauliques puissants. Même avec une puissance disponible très réduite pour l'activation, seul le contrôleur de hauteur a du être modifié pour atteindre un déplacement stable. Afin d'améliorer encore les performances énergétiques du robot, on a introduit une variable de "temps de déplacement" qui permet de faire correspondre un cycle de déplacement à un intervalle fixe, indépendamment des conditions d'opération. Cette notion nous a permis de calculer une trajectoire de référence pour la position de la patte pendant la phase de vol. Une analyse comparative de consommation énergétique du Monopod ARL confirme que notre robot est le plus efficace comparé a d'autres robots marcheurs avec son coefficient de résistance spécifique de* $\varepsilon = 0.7$ *à une vitesse de* $4.3km/hr$ $(1.2m/s)$.

Acknowledgements

First, I acknowledge the support of the Natural Sciences and Engineering Research Council of Canada who made this work possible by granting me an NSERC PGSA scholarship.

The work discussed in this thesis would not have been possible without the support of a number of people. I would like to thank Mojtaba Ahmadi for his enthusiastic attitude and his encouragement. More concretely, he coded the simulations of the ARL monopod and developed the dynamical equations used in the design of the hip actuation system. Nadim El-fata was always there to tell me what size capacitor I needed or whether a certain electronic component was destroyed. Without his good-humored attitude and willingness to untangle the mysteries of electronic design the experiments would certainly not have proceeded. I also thank Gregory Petryk who developed and implemented the XP/DCS interface for treadmill control and also installed the treadmill and planarizer. Joey Mennitto was always available when I needed someone to complain to about things going wrong. He provided a constant, moderating influence which helped me keep going. Martin Buehler is responsible for my interest in legged locomotion and without him I would certainly not have been able to work on this project. His theoretical knowledge in the field of locomotion as well as his practical experience with machines that don't always work made him not only a supportive reference but also someone with the patience and skill necessary to resolve elusive technical glitches.

Contents

List of Figures

Chapter 1

Introduction

Goals of Legged Robot Research

There are two important motivations to the study of legged robots. First, basic understanding of biological locomotion can be greatly increased through the process of reproducing animal walking and running by mechanical means. Perhaps of more practical interest is the potential performance of legged systems in rough terrains. Raibert points out, "only about half of the earth's landmass is accessible to existing wheeled and tracked vehicles, whereas a much larger fraction can be reached by animals on foot."[29]

Legged robots which are capable of dynamic operation and active balance promise to exhibit similar mobility, efficiency and dexterity as their biological counterparts. Such robots would be able to operate in a large range of environments and surface conditions and promise to be the mobile platform of choice compared to wheeled systems. However, before legged robots become practical, improved stability properties and autonomous operation are essential.

Historical Background

Legged robots generally fall into one of two classes; those capable of dynamic operation and those designed for static walking. In static walkers, stability is assured through kinematics by keeping the centre of mass of the machine within the polygon formed by the supporting feet. This requires these machines to have at least four legs although they are often built with six legs to improve mobility. Static walkers do not balance actively and since dynamics of motion are not considered, speeds are low. Dynamic operation requires that balance be actively maintained at all times. Dynamic robots, which can locomote even with a single leg, have a greater potential for speed and power efficiency.

Experimental research on actively balanced running machines began with Matsuoka [15] who built a planar one-legged hopping machine to study repetitive hopping in humans. His machine was sliding on a 10° inclined plane and thrusted by an electric solenoid. The first walking machine with active balance was built by Miura and Shimoyama [19]. It operated with stiff legs, similar to humans on stilts.

Our work has been inspired by past research of Marc Raibert [29] who has led the field of dynamically stable legged locomotion during the past decade. He built a variety of running robots, starting with a planar one-legged machine [28], followed by a 3D one-legged, a two-legged planar robot, and a quadruped. His latest robots include a 3D two-legged robot, where each leg has four actuated degrees of freedom. Except for the first one-legged planar hopper, which was pneumatically actuated, his designs use powerful hydraulic actuators and rely on pneumatics for the leg spring only. By effectively eliminating power constraints Raibert was able to focus exclusively on robot design and control issues. This strategy was eminently successful and he built many different running robots based on an almost standardized set of custom parts. It is important to realize that all of his robots are controlled by some derivative of the tri-partitioned decoupled control developed for the original one-legged planar hopper [29].

Papantoniou [23, 22] has also built a planar monopod actuated by two electric motors and is using a derivative of Raibert's controller. He employs a clutch which engages the spinning motor at maximum leg compression to maximize energy transfer to the leg. Thus for his device energy is only added during the second half of the stance phase. To make this approach work, the stance time needed to be increased considerably to $470ms$, resulting in a mode of operation he terms "compliant walk". This is different from a running gait in that the flight duration is shorter and the hopping height is shallower. The lower flight duration limits the amplitude of leg swinging and thus the running speed. There are many more research labs working on dynamic locomotion. An extensive review of research in legged locomotion can be found in [30].

Progress at McGill

Research into legged robots at McGill began in 1991 at the Ambulatory Robotics Laboratory (ARL) of McGill's Centre for Intelligent Machines (CIM). Work at ARL is directed toward understanding the theoretical and practical issues involved in robot locomotion with the final goal of building a fully autonomous, affordable quadruped capable of performing in an industrial environment. To this end, ARL's robots employ electrical actuation rather than hydraulics, since it is more suitable for indoor autonomous robots, and is a cleaner, safer and less expensive technology.

Our current planar monopod represents an important first step towards that final goal. The process of mechanical design and controller development and implementation as well as results gathered from experimental runs will prove invaluable to developing more sophisticated, multi-legged robots. Although the planar monopod may seem simple and far removed from practicality, its simplicity allows for development of analytic results as well as providing new conceptual insights, yet it displays all the relevant properties of active balance and dynamic operation.

Since autonomous operation is desired, this implies an on-board power source which increases the mass of the robot at the expense of pay load. Thus, minimizing energy consumption becomes an important consideration. Analysis of the energetics of the ARL Monopod shows encouraging results, but we feel further improvements can be realized by developing controllers aimed at minimizing energy consumption as well as stabilizing the running gait.

Author's contributions

I joined the ARL research team headed by Prof. M. Buehler in January 1993. At that time, the virtual motion system was in place [20], the robot leg (Figure 2.1) and related electronic hardware had been constructed, and preliminary control software was written [33]. Experimentation had yet to begin. By early February, after becoming familiar with the system I performed stable vertical hopping experiments with the leg. I next performed experiments to evaluate the torque-speed characteristics of our actuators. These results are given in Section 2.1.3 and led to the development of an analytically tractable, exactly implementable open-loop torque controller used to stabilize the hopping height [27]. This controller is described in Section 3.1.

In the spring and summer design and construction of a body and actuated hip for the ARL monopod proceeded (Section 2.2). I was responsible for this detailed mechanical design and construction although the analysis involved in sizing the hip transmission components was done in collaboration with M. Ahmadi. In September, I used Raibert's work was the basis for writing control software for the monopod. On September 20 I performed the first stable, 2D running experiment with the ARL monopod on the treadmill. Experiments continued through October and by the beginning of November the robot was running at a top speed of $1.2 m/s$ on the treadmill. These results, originally reported in [11], are described in Section 4.2.

Through a detailed analysis of the energetics of our robot as well as a survey of other legged robots [12], I established that the ARL Monopod has the lowest specific resistance in among powered legged vehicles (Section 4.3).

We developed a scalar "locomotion time" variable as a tool for new control ideas and implemented calculation of this locomotion time online during an experimental run. I used this locomotion time as the basis for calculating a reference trajectory in leg angle. Implementing this reference trajectory during an experimental run makes the leg swinging smoother and minimizes jolting at lift-off and touchdown.

In an attempt to improve the quality of sensor data, I developed, constructed and tested a *hybrid angle sensor* design based on analog sensing and local A/D conversion. The quality of sensor data has a direct effect on controller performance. This sensor consists of an analog potentiometer coupled to an on board A/D converter circuit with active filtering and a scalable input range (Section 5.2.3).

Organization of the thesis

The thesis is organized as follows. Chapter 2 discusses the experimental hardware and describes issues related to mechanical design of the ARL Monopod. Control issues for the robot are discussed in Chapter 3. In Chapter 4 the experimental procedure and results obtained are described. A detailed energetic analysis of robot locomotion as well as a comparison of robot efficiency to that of other land vehicles is also included in Chapter 4. Chapter 5 describes proposed control strategies and mechanical design modifications aimed at improved energy efficiency. In Chapter 6 future work is proposed.

Chapter 2

Planar Running Robot

2.1 Hardware Description

2.1.1 ARL Monopod

The ARL Monopod may be described as a prismatic, planar, electric monopod. It is composed of a leg with a sliding prismatic knee joint and a mechanical spring. The leg attaches to a body through an actuated hip joint. Mechanical design considerations for the leg in Figure 2.1 are discussed in [27].

The layout of the monopod is shown in Figure 2.4. The robot has six degrees of freedom (DOF) of which only two are actuated. Actuation comes via two 80W brush DC motors (Maxon 2260 series) powered by PWM servo amplifiers (Galil MSA-12-80). The servo amplifiers operate in current feedback mode allowing motor torque to be specified directly. The motors each drive a high efficiency NSK ball screw. One ball screw compresses the leg spring while the other actuates a cable-pulley transmission to control the hip angle (leg relative to body). The cables can optionally be replaced with compliant elements. Optical encoders are used to sense motor positions and hip angle. A potentiometer is used to measure the leg length. All positions are differentiated and filtered in software using a first order Infinite Impulse Response (IIR) filter to obtain rates. Filtering is necessary to eliminate sensor noise due to quantization of encoder signals and electromagnetic interference (EMI) between high-current, high-bandwidth motor power signals and analog sensors.

2.1.2 Virtual Motion System (VMS)

The Virtual Motion System [20] consists of a treadmill and planarizer that constrain robot motion to a vertical plane. The planarizer employs horizontal and vertical ball slides riding on precision ground rods to allow free movement in the horizontal and vertical directions. The body of the robot attaches to the planarizer through a revolute joint which uses angular contact ball bearings to allow free body pitching. All three DOFs are instrumented with optical encoders to measure the horizontal and vertical position and the body pitch angle. Treadmill power comes from a $3.7kW$ DC motor controlled by a regenerative DC motor controller with manual setpoint adjustment. The treadmill allows unlimited range for robot running. A wrangle is attached to the planarizer so the robot may be manually lifted off the treadmill in case of emergency.

2.1.3 Motor Model

The motors which actuate the leg spring and hip angle behave like ideal "torquers," that is, we can control instantaneous current up to the thermal and operational limits imposed by the motor construction and the drive electronics. Since we operate intermittently we are able to draw the maximum stall torque of 1.78 Nm and utilize the operational regime for short term operation in the first quadrant given by the manufacturer (Figure 2.2).

The servo amplifiers are powered from a $48V$ unregulated power supply allowing the motor's stall torque of $1.8Nm$ to be reached. The resulting operating regime is shown in Figure 2.2, which was obtained experimentally by commanding a desired torque square wave profile between $+1.8Nm$ and $-1.8Nm$. For this class of fractional

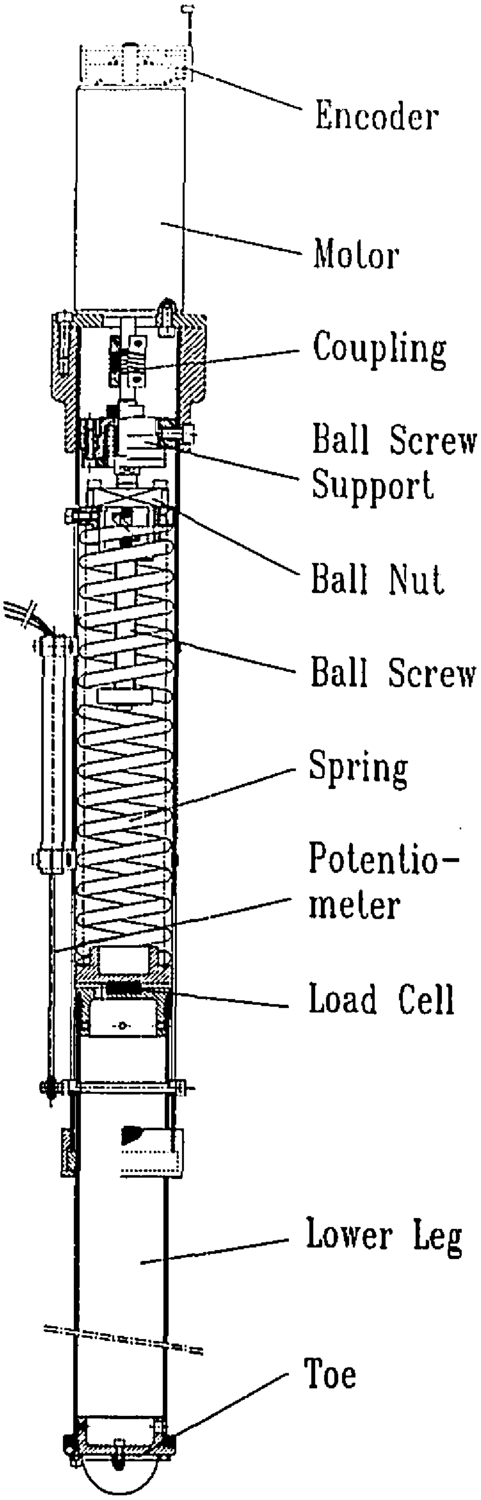

Figure 2.1: *Leg Assembly*

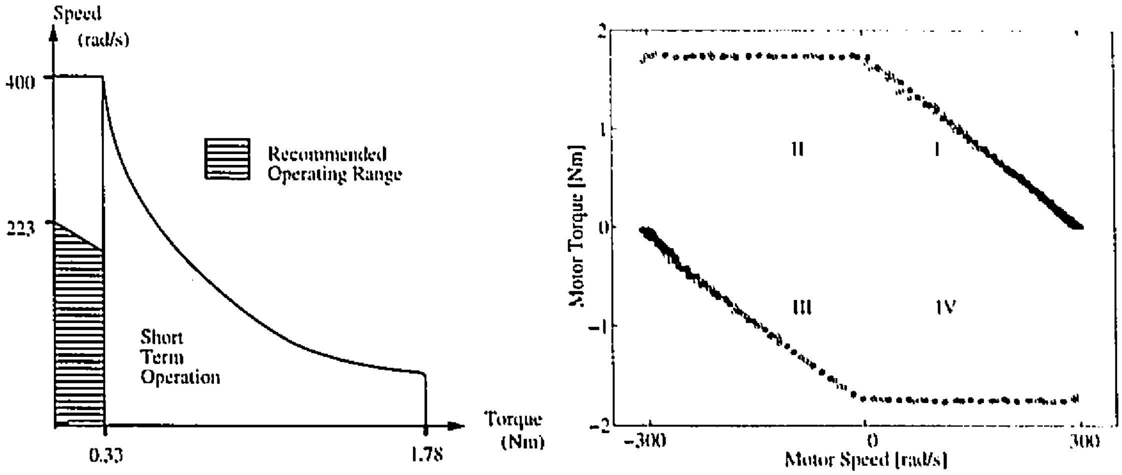

Figure 2.2: *Torque speed curve of the Maxon 2260 series brush 80W DC motor, adapted from [2] (left), and experimental torque speed curve (right). The torque was limited to* $\hat{\tau} = 1.8Nm$ *during all experiments as specified by the manufacturer.*

horsepower motors, torque is limited by

$$\tau \begin{cases} \leq \hat{\tau}(1 - \frac{\omega}{\hat{\omega}}) & \text{First quadrant} \\ \leq \hat{\tau} & \text{Second quadrant} \\ \geq -\hat{\tau}(1 + \frac{\omega}{\hat{\omega}}) & \text{Third quadrant} \\ \geq -\hat{\tau} & \text{Fourth quadrant} \end{cases} \quad (2.1)$$

where $\hat{\tau}$ is the stall torque and $\hat{\omega}$ is the no load speed. It is therefore evident that the traditional actuator limit of the form

$$\|\tau\| \leq \hat{\tau}$$

is not applicable to this class of electric DC motor which is increasingly common for driving small to medium size robots and mechanisms.

2.1.4 Electronic Hardware

Figure 2.3 shows how the electronic hardware relates to the monopod. A single XP/DCS Transputer node [1] is used to read and process sensor signals, compute states and control outputs, log data, and interface with the servo amplifiers. The standard XP/DCS Transputer board is connected to a custom I/O board which links the robot hardware (sensors and servo amplifiers) to the XP/DCS board. This custom I/O board performs analog to digital data conversion for sensors and servo amplifier feedback signals, quadrature decoding of raw encoder signals, digital to analog conversion of controller output signals and provides reference voltage for potentiometers through a DC-DC converter. These devices are housed in a rack next to the VMS and connect to the robot through a series of cables.

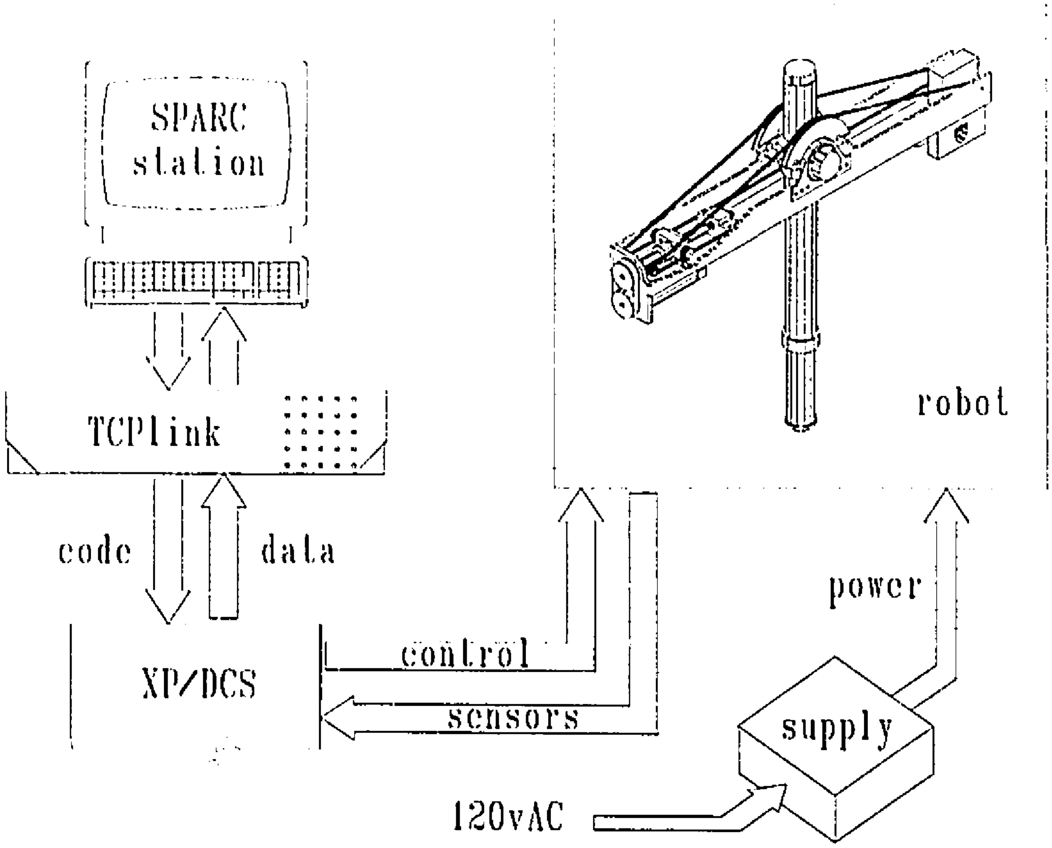

Figure 2.3: *Electronic Hardware Connection Diagram*

Software is developed and compiled on a SPARCstation and downloaded through an Ethernet gateway (IMS B300 TCPlink) to the XP/DCS board before an experimental run. There is no communication between the XP/DCS and the SPARCstation during the run when the Transputer runs the software described in Section 2.1.5 at a rate of $1kHz$. After the experiment is completed, logged data is downloaded to the SPARCstation for offline analysis.

Power for the robot comes from the grid through a single Galil CPS-6-48 unregulated DC power supply which feeds both servo amplifiers. The servo amplifiers can handle up to $2kW$ peak throughput and servo the motor current (and thus the motor torque) at a $2.5kHz$ closed loop bandwidth.

2.1.5 Software

The control algorithms discussed in Chapter 3 are coded as part of a 1300 line C program which controls all robot functions. This software consists of an initialization routine, a main loop and a data recovery routine which downloads data from the Transputer memory to the SPARCstation for offline analysis following the experimental run. The main loop is executed once every millisecond and performs the following functions:

- keeping track of real time used to compute time dependent physical quantities and to synchronize the controller frequency,
- reading raw sensor data through the I/O board,
- processing raw sensor data into usable form including differentiation and filtering of position data to obtain rates,
- maintaining a watchdog timer signal which acts as a failsafe; the treadmill and servo amplifiers are disabled when this signal is not present,
- controlling an audible alarm which informs the operator of the beginning and end of an experimental run,
- computing the current state of the robot (flight, stance, etc) from sensor signals,

- running the control algorithms to determine desired torque values,
- sending desired torque values to the servo amplifiers which control and power the motors, and
- recording sensor and state data into an array for later recovery into the SPARCstation; these data are typically recorded every 15 milliseconds for a 60 second run.

This software is developed and compiled on the SPARCstation and is loaded into the Transputer just prior to an experimental run.

2.2 Design of Body and Actuated Hip

2.2.1 Mechanical Layout

Running in the plane demands the leg be able to swing fore and aft in a controlled fashion. This in turn implies an actuated hip joint attaching the leg to the robot body. The inertia of the body should be high compared to that of the leg in order to minimize the pitching motion of the body in response to leg swinging. At the same time, body mass should be kept low to keep energy requirements for vertical motion small. Both requirements can be satisfied by having a long body whose mass is concentrated at the ends. The body of the monopod consists of a standard aluminum channel section used for structure. Elements of the hip actuation system (hip motor, ball screw, servo amplifiers) and a $2kg$ counterweight (to offset the hip motor and ball screw masses) are housed at either end of the body to increase the body inertia. The final design shown in Figure 2.4 also keeps the gravity centre of the robot at the same height as the hip joint. No attempt was made to minimize the weight of the channel section which alone accounts for 1/4 of the robot's $15kg$ mass. In future, reducing the body mass and eliminating the counterweight could allow the XP/DCS board and an electro-chemical battery to be placed on the body for autonomous running experiments.

In order to minimize requirements for spare parts we decided to use the same type of motor for hip actuation and leg actuation. The $1.8Nm$ stall torque of these $80W$ motors along with the $55Nm$ hip torque required for forward running demand a 30:1 transmission gear ratio. Moreover, the transmission design should allow for the insertion of a compliance in series with the hip actuation system. This compliance is required for the experimental study of passive dynamic running currently being investigated in simulation.

By using a cable and pulley system to actuate the hip joint, such a series compliance can easily be incorporated into the design by including extension springs in the long cables. Figure 2.4 shows these cables (4) fixed at one end to the hip pulley (3) which actuates the leg (12). At the other end, the cables run over idlers (9) and attach to the ball nut of a high efficiency NSK ball screw (6, 5). The ball screw is actuated by the hip motor (8) through a miniature HTD timing belt (10) and unity ratio pulleys and converts motor torque into an axial force delivered at the ball nut. This ball nut force, in turn, tensions the cables which actuate the hip pulley.

Using the HTD belt to relate the motor to the ball screw results in a compact assembly with the motor placed underneath the ball screw and permits a body length of only $0.9m$. In addition, the HTD belt provides some protection for the motor by isolating it from shock loads. The hip pulley radius and ball screw lead were selected as described below in Section 2.2.2 to give the required gear ratio of 30:1.

2.2.2 Hip Transmission Design

This section describes an optimization procedure for selecting the parameters of the hip actuation system. The dynamical equations of the hip transmission system shown in Figure 2.5 were derived and simulated by M. Ahmadi. This simulation forced the leg angle to follow a desired trajectory similar to the expected trajectory for robot

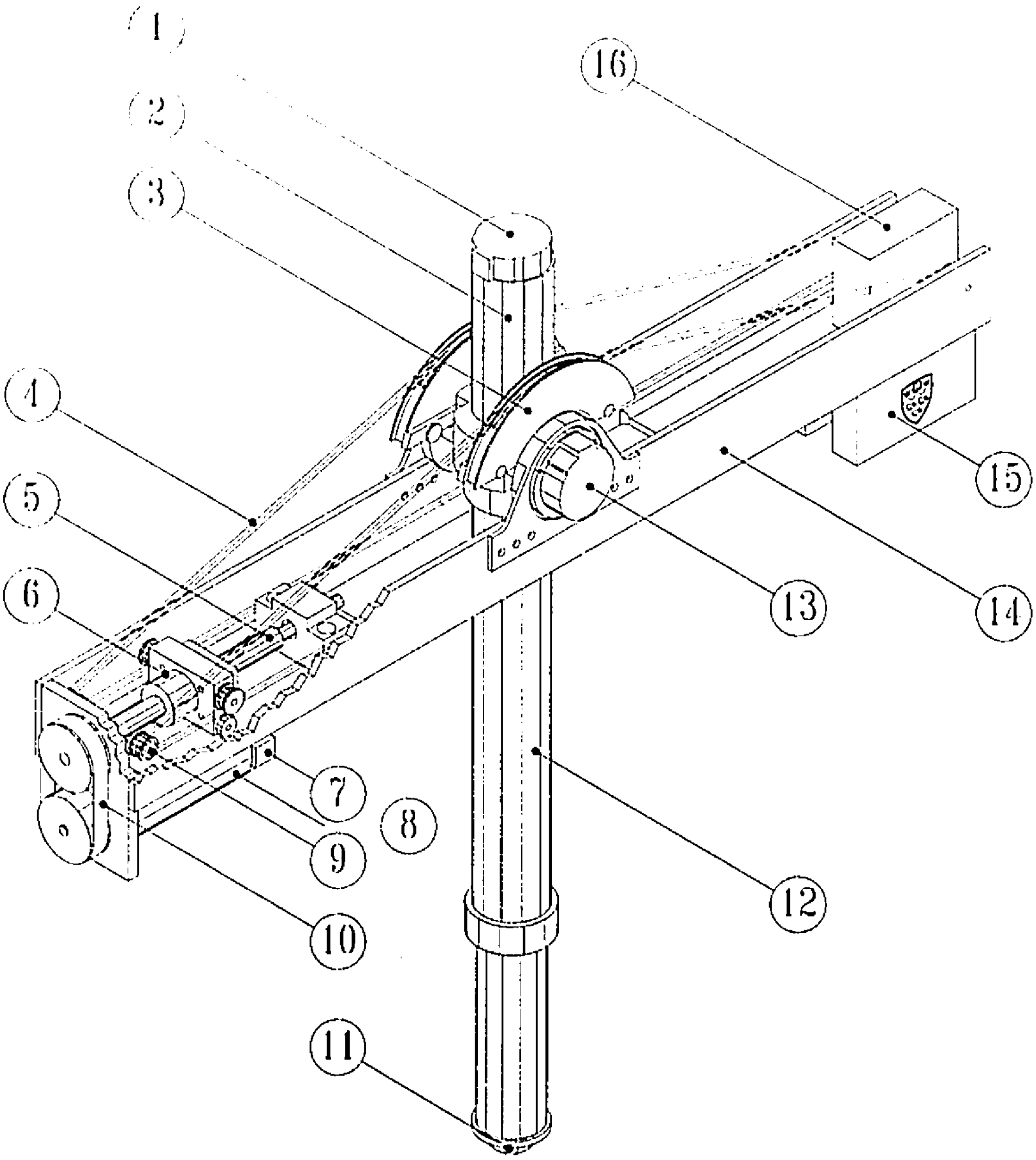

1	leg motor sensor	7	hip motor sensor	13	hip sensor
2	leg motor	8	hip motor	14	body
3	hip pulley	9	cable idler	15	servo amplifiers
4	cables	10	timing belt	16	counter weight
5	ball screw	11	rubber toe		
6	ball nut	12	leg		

Figure 2.4: *Legged Robot Assembly*

running.

The free parameters in the hip transmission design are the pulley radius R, the ball screw lead r_s (equivalently L in mm/rev) and the hip compliance stiffness k_h. For direct actuation, k_h is set to a large value equal to the cable stiffness. The design requires that the motor stall torque not be exceeded ($\tau_m \leq \hat{\tau}$) while the leg swings during running. A sinusoidal trajectory was used to represent the motion of the leg during running. Results from vertical hopping experiments performed with the robot leg [27] were used to estimate the parameters of this sinusoidal trajectory. A frequency of $2Hz$ equal to the vertical hopping frequency and an amplitude of 20° corresponding to a running speed of $0.9m/s$ were selected. Body pitching was neglected.

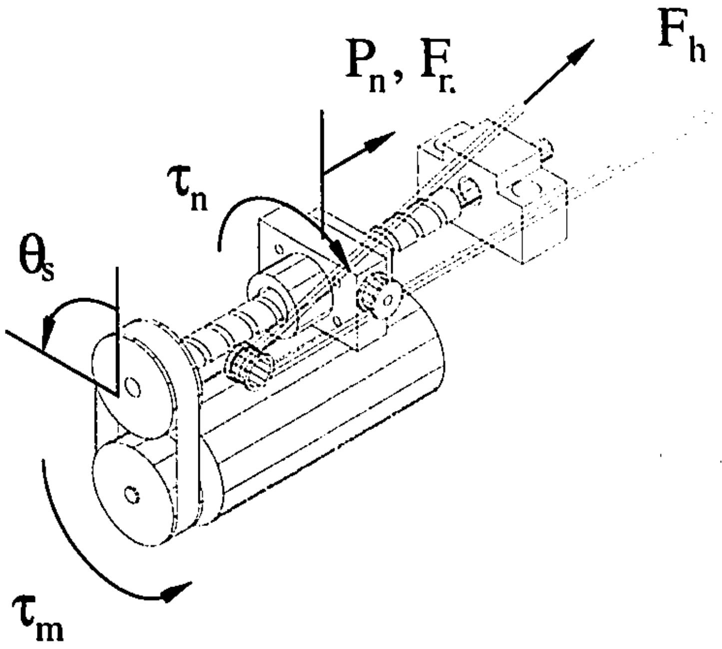

Figure 2.5: *Hip Transmission Diagram*

The variables involved in the dynamical equations of the hip actuation system are given in Table 2.1 and are graphically represented in Figure 2.5. By balancing forces in the hip actuation system, the dynamical equations may be obtained. Since a unity ratio transmission connects the hip motor to the ball screw, the hip motor torque, τ_m, is equal to the ball screw torque. This torque goes into acceleration of the ball screw

R	hip pulley radius	(m)
θ	hip joint angle	(rad)
C_h	hip joint damping	$(N/m/s)$
k_h	hip compliance stiffness	(N/m)
c_h	hip compliance damping	$(N/m/s)$
F_h	hip cable tension	(N)
τ_m	hip motor torque	(Nm)
θ_s	ball screw angle	(rad)
r_s	ball screw lead	(m/rad)
J_s	ball screw inertia	(kgm^2)
p_n	ball nut position	(m)
m_n	ball nut mass	(kg)
F_n	ball nut force	(N)
τ_n	ball nut torque	(Nm)
m_l	leg mass	(kg)
J_l	leg inertia	(kgm^2)
l_c	distance from leg CG to hip joint	(m)
g	gravitational acceleration	(m/s^2)

Table 2.1: *Transmission Variables*

as well as balancing the ball nut torque, τ_n, according to the relation

$$\tau_m = J_s\ddot{\theta}_s + \tau_n$$

where τ_n relates to the force in the ball nut, F_n through the lead of the ball screw, r_s,

$$\tau_n = F_n r_s.$$

The force in the ball nut is used to tension the hip cables for actuation as well as accelerating the ball nut itself;

$$F_n = F_h + m_n\ddot{p}_n.$$

The linear acceleration of the ball nut, $\ddot{p}_n$ relates to the angular acceleration of the ball screw, $\ddot{\theta}_s$, through the ball screw lead,

$$\ddot{p}_n = r_s\ddot{\theta}_s.$$

Taken together, the above equations reveal the motor torque relation

$$\tau_m = r_s F_h + \alpha_h\ddot{p}_n \tag{2.2}$$

where

$$\alpha_h = J_s/r_s + r_s m_n$$

accounts for the combined inertia of the ball screw and ball nut.

The tension in the hip cable, F_h, balances the dynamic load of the hip compliance,

$$F_h = 2k_h(R\theta - p_n) + 2c_h(R\dot{\theta} - \dot{p}_n), \tag{2.3}$$

and, so, approximating $sin(\theta) \approx \theta$ for small angles, the dynamics of the actuated hip are represented as

$$J_l\ddot{\theta} = RF_h - C_h\dot{\theta} - m_l g l_c\theta. \tag{2.4}$$

Solving equation (2.4) where the leg angle θ follows the sinusoidal path $\theta = \theta_0\sin(\omega t)$ gives the motor torque

$$\tau_m = A\sin(\omega t) + B\cos(\omega t) \tag{2.5}$$

where A and B are functions of the system design parameters, primarily the lever arm R, the stiffness k_h and ball screw lead r_s, as well as the parameters of the leg trajectory. We can now evaluate the motor's torque requirements as a function of leg speed, $\tau_m(\omega)$. The peak motor torque, τ_{max}, depends on the design parameters in a simple fashion,

$$\tau_{max} = \sqrt{A^2 + B^2}. \tag{2.6}$$

This maximum torque is shown in figure Figure 2.6 for the direct actuation case with a leg angle trajectory of amplitude $\theta_0 = 0.35rad$ and frequency $\omega = 4\pi rad/s$. The maximum motor torque, τ_{max} is plotted against the ball screw lead, L, expressed in mm/rev for three values of pulley radius $R = 0.04m$, $R = 0.08m$, and $R = 0.14m$.

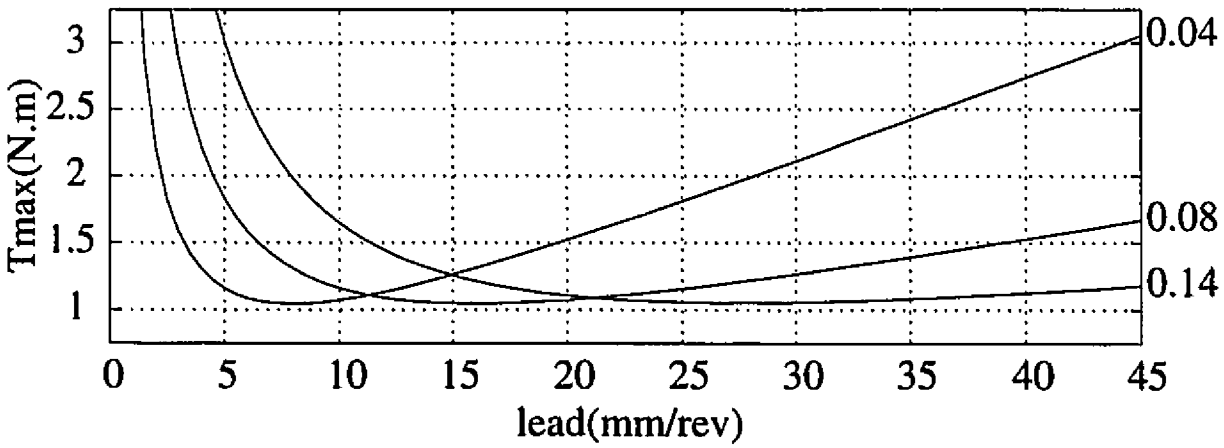

Figure 2.6: *Hip Transmission Design. The ordinate shows the maximum hip motor torque required to swing the leg through a reference trajectory with a given combination of ball screw lead and pulley radius. The final design uses lead = 16mm/rev, radius = 0.08m.*

The next step in the design process is to select the optimal combination of ball screw lead and pulley radius from Figure 2.6. Unfortunately, this problem cannot be cast as a straightforward numerical minimization problem, since there are many non-standard constraints. For example, the motor characteristics require that the maximum torque be a function of the velocity given by equation (2.1). Furthermore ball screws are available only in coarsely discrete leads and lengths and their inertial parameters are only available via lookup tables.

The generated cable tension F_h should be kept small since it affects the overall size and weight of our structures. Since we plan to use elastomeric springs, the spring stiffness is limited to $5kN/m$ due to energy storage limitations. The ball screw travel should be less than $0.1m$ to limit the inertia, mass and body length. The design is further complicated by the necessity to meet the constraints for both direct and compliant actuation. The compliant case is facilitated by large pulley radius R, resulting in smaller torque requirements, but this increasing R, when combined with the optimum lead (Figure 2.6), increases motor velocity, acceleration, ball screw travel, and ball screw lead in the direct actuation case.

The final design parameters of lead $L = 0.16mm/rev$, pulley radius $R = 0.08m$ and spring constant $k_h = 3600N/m$ are an attempt to satisfy all the constraints concerning pulley radius, ball screw lead, and maximum motor torque and velocity. Together with a ball screw travel of $0.13m$, this configuration allows a maximum hip angle of $\pm 45°$. This set of parameters minimizes the motor torque-speed requirements for compliant running by matching the natural frequency of the system with the frequency of the vertical oscillations of $2Hz$ [27].

Chapter 3

Control

3.1 Three-part Decoupled Control

Running for a single legged system is comprised of a *stance phase* during which the toe is in contact with the ground and a ballistic *flight phase* when the toe is off the ground and the robot behaves as a projectile. These phases are illustrated in Figure 3.1. A *step* comprises one stance phase between *touchdown* and *lift-off* of the toe, and one flight phase beginning with *lift-off* and ending at the next *touchdown*.

Raibert developed a control strategy for legged robots which decouples the complex coordinated running motion into three separate tasks; *hopping height control, forward speed control,* and *attitude control.* Hopping height is controlled during stance using the leg actuator while body attitude is simultaneously controlled using the hip actuation system. During flight, the hip actuator controls forward speed. In order to control the running motion of our robot, we took Raibert's three part control algorithm [29] and applied some hardware specific modifications as described below.

3.1.1 Vertical Motion (Hopping height control)

In Raibert's running experiments he stabilized the vertical motion of his machines by specifying a constant position step to the leg actuator during stance at the instant of

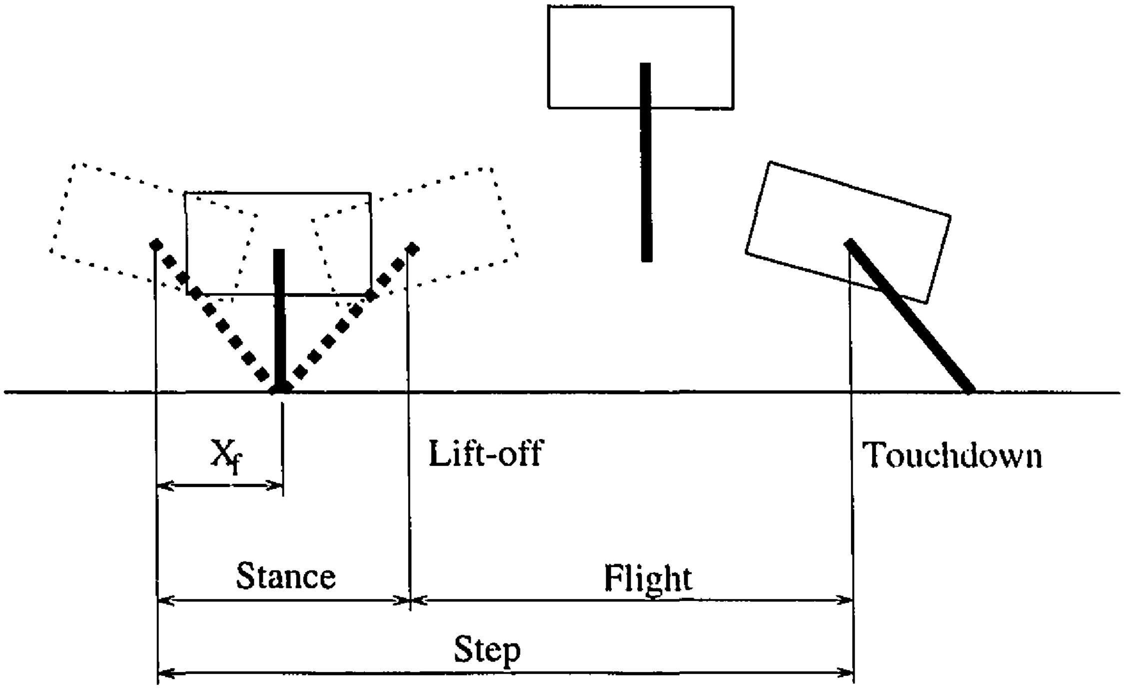

Figure 3.1: *Phases of Robot Running*

maximum leg compression. In response to this step, the actuator lengthens, thrusting the body upward and injecting energy into the system. The magnitude of this actuator position step determines the steady hopping height.

For the ARL Monopod, the ground force acting against the leg actuator at maximum compression is approximately $500N$, which makes the position step an impractical strategy with low power electric actuators. Instead we use a different open loop controller described in [27],

$$\tau = \bar{\tau}(1 - \frac{\omega}{\hat{\omega}}), \tag{3.1}$$

which specifies a scaled version of the maximum torque-speed curve of our motor, equation (2.1), with $0 \leq \bar{\tau} < \hat{\tau}$ in the first quadrant (stance), and a high gain PD controller to return the actuator during flight. This strategy is exactly implementable and applies thrust continuously during the entire stance phase. For our experiments we chose $\bar{\tau} = 1Nm$ where $\hat{\tau} = 1.8Nm$. By applying actuator effort throughout the entire stance phase rather than only at the time of maximum compression, the power requirement for actuation is greatly reduced. As in Raibert's experiments, there is a stable hopping height which corresponds to each value of $\bar{\tau}$.

3.1.2 Foot Placement Algorithm, FPA (Speed control)

When the robot hops with zero forward speed, the toe should obviously be placed beneath the gravity centre (CG) of the body to keep the robot from falling over. However, when running with non-zero speed, the body moves forward over the toe during the stance as seen in Figure 3.1. The CG of the body moves forward a distance equal to the product of forward speed and stance duration ($\dot{x}T_s$). In this case, where should the toe be placed for stability? Raibert states that for each running speed, there exists a *neutral point* given by

$$x_{fo} = \frac{\dot{x}T_s}{2}$$

which is the touchdown toe position measured forward from the body CG that causes zero net acceleration. When, at the end of a flight phase, the toe touches down at the neutral point the body moves symmetrically over the toe position through stance and the next lift-off speed equals the last touchdown speed. If the toe touches down behind the neutral point, the body accelerates forward; placing the toe ahead of the neutral point slows the body down. There is an analog to this behavior in human runners who lean forward while accelerating and lean back to slow down.

The neutral point is the key to Raibert's foot placement algorithm (FPA) which determines the touchdown position of the toe relative to the body CG (shown in Figure 3.1) by the relation

$$x_f = \frac{\dot{x}T_s}{2} + \kappa_{\dot{x}}(\dot{x} - \dot{x}_d)$$

where $\kappa_{\dot{x}}$ is an empirically tuned gain and $\dot{x}_d$ is the desired running speed.

Since our robot runs on a treadmill, the treadmill speed $\dot{x}_{TM}$ replaces $\dot{x}$ in Raibert's FPA. It was also necessary to add an "integral" term to keep the robot near the center of the treadmill. Without this integral term any steady state speed mismatch between the robot and the treadmill would cause the monopod to exceed the travel limits of the VMS. The FPA implementation for our robot is thus given by

$$x_f = \frac{\dot{x}_{TM} T_s}{2} + \kappa_x (x - x_d) + \kappa_{\dot{x}} (\dot{x}_{TM} - \dot{x}_d) \tag{3.2}$$

where x is the robot's position relative to the centre of the treadmill, x_d and $\dot{x}_d$ are the desired position on the treadmill and desired running speed, respectively, and κ_x and $\kappa_{\dot{x}}$ are empirically tuned gains.

Simple geometry converts the desired touchdown toe position x_f into a desired leg angle. Taking into account the body pitch, a setpoint is obtained for the hip actuator which places the toe at the desired position.

3.1.3 Body Attitude (Pitch control)

Since the hip actuator servos the toe position throughout the flight phase, the robot body pitches freely during this time. Following touchdown, the leg swings backwards due to the forward momentum of the robot body. Thus, the hip actuator can be used during stance to regulate the pitching motion of the robot body. Raibert used a simple PD controller to compute the torque of the hip actuator, τ, necessary to keep the robot body steady and horizontal,

$$\tau = \kappa_p (\phi_d - \phi) - \kappa_d \dot{\phi},$$

where ϕ_d is the desired hip angle, ϕ and $\dot{\phi}$ are the hip angle and rate, respectively, and κ_p is an empirically tuned gain. This controller remained unchanged for our experiments.

3.2 Low-level Servos

The high level controllers described above are used to determine setpoints for the actuators. However, to ensure stable running, low level servos are needed which can reproduce these desired positions. In the case of back driving the leg actuator during flight as well as servoing the hip actuator during flight for the FPA and during stance to regulate body pitching, proportional plus derivative (PD) control laws have been selected for there simplicity and excellent performance characteristics.

The gains for these controllers are empirically tuned and can be easily set even in the absence of a good physical model of the system. For the experimental runs, PD gains were set by demanding a step in position and observing the recorded sensor data. The proportional gain was increased up to the limits of system stability dictated by motor torque limits and sensor signal noise. This reduces the rise time of the system. Next, the derivative gain was tuned to minimize overshoot. The system was then tested in response to sinusoidal inputs of differeing frequencies and the gains were fine tuned in order to ensure accurate tracking of desired positions.

The stringent requirements for tracking performance and response rate force high controller gains, almost at the limit of system stability. These necessarily high gains when combined with noisy sensor data can lead to large amplitude, high bandwidth torque variations which increase the overall energy requirement for robot running.

Chapter 4

Experimentation and Results

4.1 Experimental Procedure

The experiments discussed in this chapter were performed using the ARL Monopod and ancillary hardware described in Chapter 2.

4.1.1 Start-up

The running experiments are performed by a single operator. At the beginning of each experiment, the operator manually adjusts the body to be perpendicular to the leg and balances the robot in its unstable equilibrium position as shown in Figure 2.4. The robot now supports itself in this position while the operator downloads the executable software (Section 2.1.5) from the SPARCstation to the XP/DCS. The software starts up and initializes all variables to zero except the body height variable which is set according to the initial reading from the leg length sensor. This reading accounts for the unknown compression of the leg spring. Next, the XP/DCS sounds an alarm to signal the start of the control loop. The state machine is set to START and waits for the first flight phase. The operator lifts the robot about $50mm$ off the treadmill using the wrangle to initiate the first flight phase, then drops the robot. The robot now functions autonomously and the wrangle is only used again at the end of the run.

4.1.2 Treadmill Control

Vertical hopping is initiated with the treadmill stopped. After a few steps the hopping height becomes stable and the operator starts the treadmill. Although the treadmill speed is sensed by the controller, the speed setpoint is adjusted manually by the operator. This means that no two experiments have the same velocity profile and so it is more difficult to compare results from separate experiments since periods of similar treadmill speed must first be located before data can be compared.

Figure 4.1 shows the treadmill speed recorded over three successive steps during robot running. The figure clearly shows fluctuations of approximately 5% in the treadmill speed. The amplitude of these fluctuations is approximately constant with running speed and appear larger for slower running. At touchdown, the robot transfers its weight to the treadmill which is unloaded during flight. This load on the treadmill is roughly equal to the force in the leg spring which peaks about halfway through stance when the spring reaches its maximum compression. The slow down in treadmill speed corresponds to this increased load. Although the $3.7kW$ treadmill motor should be able to compensate for the increased friction caused by the $500N$ load, the industrial controller which servos the treadmill speed seems unable to respond to the changing loads. While the speed shown in the figure is measured using an optical encoder, the controller uses the sensed armature voltage of the motor to detect motor speed. This is a much noisier signal which cannot easily be used to detect small-amplitude, rapidly-varying speed fluctuations.

Since the control algorithm for forward speed given in equation (3.2) depends on the treadmill speed, better control of this speed is desirable. Moreover, having control over the treadmill speed profile would prove useful for comparing different experiments. These issues have motivated the development of a software based controller for treadmill speed. G. Petryk constructed a hardware interface for the existing treadmill controller which allows the XP/DCS to assign setpoints for treadmill speed or directly for treadmill motor torque. We hope to improve the frequency response of

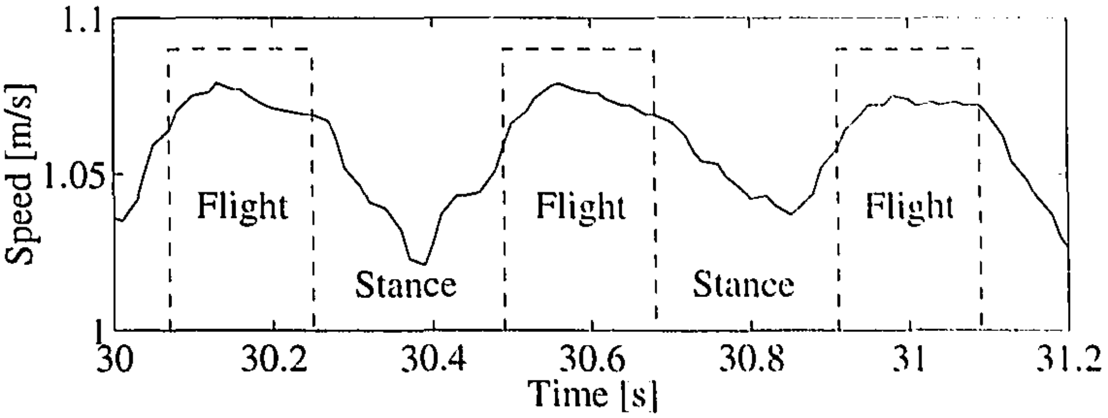

Figure 4.1: *Fluctuations in treadmill velocity during robot running. The speed is slowest when the load is greatest about halfway through stance.*

treadmill control over what is now available from the industrial controller. Testing and evaluation of the new controller is not yet complete and all experimental results for robot running reported here were obtained using the manually controlled speed setpoint.

4.2 Experimental Results

Experimental results regarding vertical hopping experiments are reported in [27]. This section reports on planar running experiments performed using the control laws presented in Chapter 3. A summary of these results has been published in [11].

4.2.1 Position Tracking

The first planar experiments were performed with zero treadmill speed. The results shown in Figure 4.2 were obtained using the position setpoint term x_d of the foot placement algorithm described by equation (3.2) to generate steps in desired forward position. The figure shows the robot position (solid curve) successfully tracking position steps on the order of one third the leg length (dashed curve). Although the dynamics of the system are nonlinear and intermittent, good tracking performance is realized using a simple proportional control law.

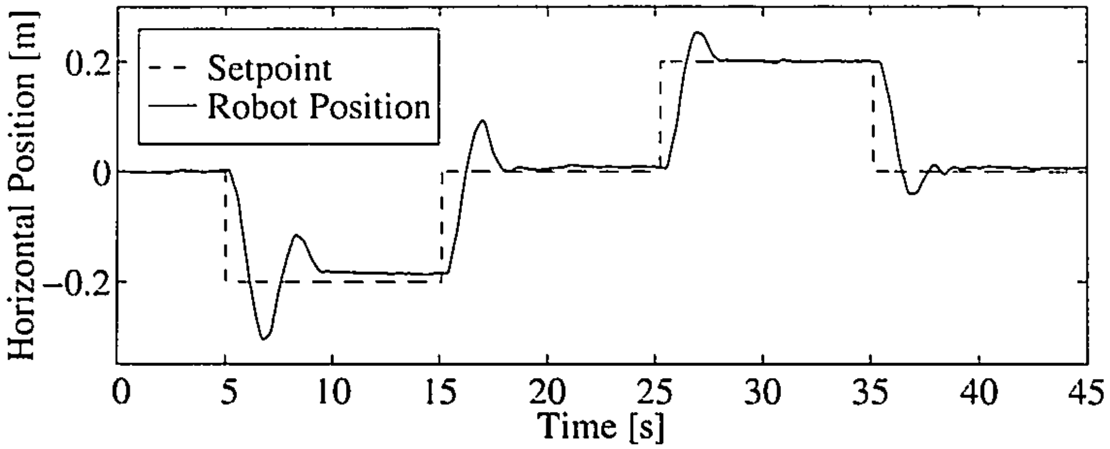

Figure 4.2: *Horizontal position regulation. The ARL Monopod tracks position steps equal to 1/3 the leg length. The dashed curve shows the setpoint.*

In addition to validating the design of the body and hip actuation system (Section 2.2) these experiments allowed the empirical position gain κ_x to be set. This same setting ensures that the robot is near the treadmill centre when the treadmill speed is non-zero.

4.2.2 Velocity Tracking

While Figure 4.2 shows that the foot placement algorithm successfully tracks position steps, the true utility of this control law is for velocity tracking. Figure 4.3 presents experimental data for robot running on the treadmill using the FPA of equation (3.2) to control forward speed. Once vertical hopping is achieved, the treadmill speed is slowly increased to a maximum of $1.05 m/s$, held steady for about $10 s$, and then reduced back to zero. The variations in the upper treadmill speed signal were discussed in Section 4.1.2.

The lower curve presents the robot position relative to the treadmill centre. The robot stays within $0.2 m$ of the desired position despite the changing treadmill speed.

Such a position deviation is small compared to the total distance travelled which is $26m$. The position error increases following step changes in the treadmill speed although even when this speed is constant the robot position oscillates. This unsteady behaviour may be due to the variations in treadmill speed discussed above since the FPA uses this speed as a setpoint. Alternately, sensor noise could account for some of the disturbances.

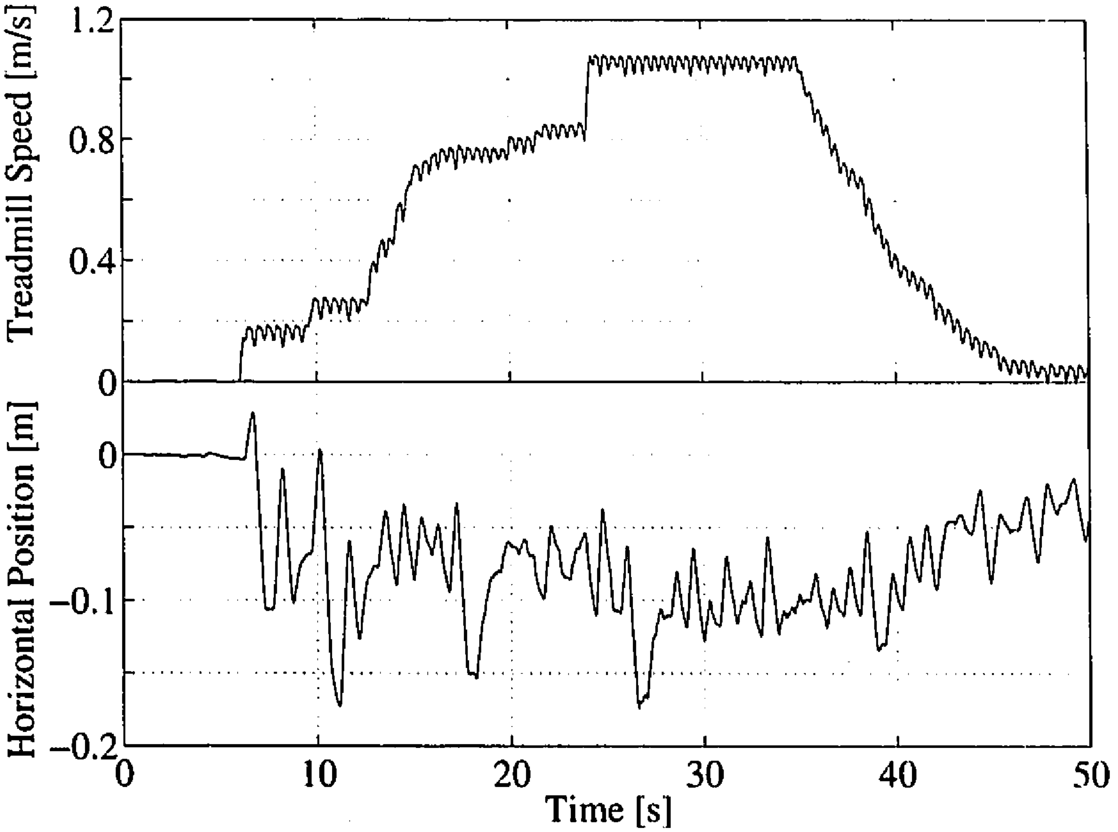

Figure 4.3: *Velocity Tracking. The treadmill speed is manually adjusted from zero, vertical hopping, to* $1.05m/s$ *and back to zero (upper curve). The lower curve shows the robot staying within* $0.2m$ *of the centre of the treadmill.*

4.2.3 Pitch Regulation

The hip actuation system can only affect the relative angle between the body and leg of the monopod. This means that in order to control the flight phase leg angle crucial to forward speed control, regulation of body pitching must be given up. Unfortunately, due to its large inertia, any instability in the body pitching motion can quickly destabilize the entire running cycle. Thus control of body pitching during the stance phase is critical to stable running. Control of this motion is achieved with the simple PD controller described in Section 3.1.3.

The lower curve of Figure 4.4 shows the cyclic oscillations of the robot body (lower solid curve) as the forward speed (upper curve) increases to $0.97 m/s$. The forward speed setpoint equal to the lift-off treadmill speed is plotted here as the robot running speed since we have shown in Section 4.2.2 that the robot tracks the speed setpoint. Despite the large variation in speed, the pitching oscillation of the robot body is kept within only $2\frac{1}{2}^\circ$ of the horizontal throughout the entire run. The pitch angle shows spikes corresponding to step increases in running speed. These perturbations are more pronounced at lower speeds when the treadmill first starts. As the speed increases, the pitching motion seems to settle into a rhythm which is less sensitive to this abrupt speed changes.

4.3 Energetics

The use of low power electric motors for actuation distinguishes the ARL Monopod from many other legged machines which use hydraulics. This low-power approach to actuation motivates a detailed energetic study of the motion of our robot. How much energy is used for robot locomotion? How is this energy related to running speed? The answers to these questions should provide insights useful to improving the energetic performance of the robot. Moreover, much of what is learned here about how this particular robot uses energy may be more generally applied in the mechanical design

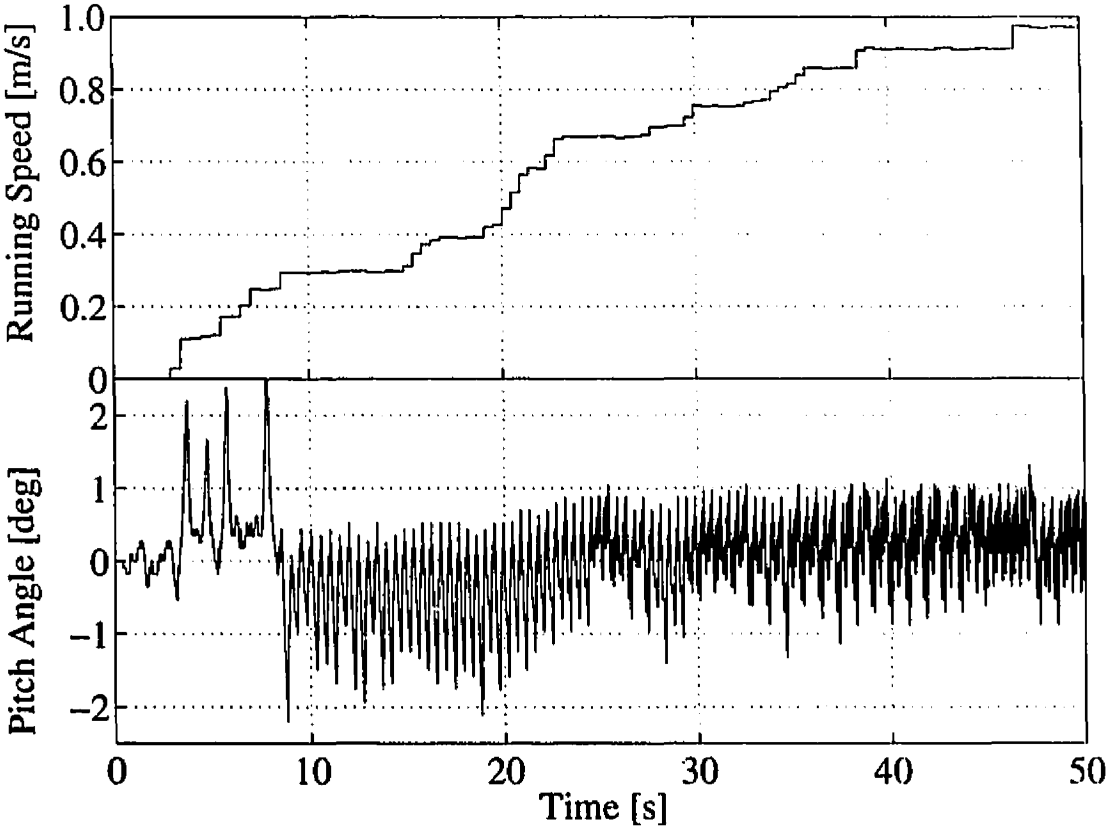

Figure 4.4: *Body pitching during robot running. The cyclic pitching motion of the robot body about the hip is kept to an amplitude of* $2\frac{1}{2}°$ *(lower curve) while the robot speed increases to* $0.97m/s$ *(upper curve).*

and controller development of future legged machines.

4.3.1 Energy Estimation

This section deals with mechanical power and mechanical energy delivered to the system by the leg and hip motors. This shaft power is the mechanical output of the motor and is distinguished from power consumption which measures the input electrical power necessary to produce the same motion. The two quantities are related by the motor efficiency which is usually not available as a function of torque and speed. Output power is a conventional measure of vehicle performance but is studied here instead of input power since it can easily be computed from the available data. It is also useful to determine the output power requirements for the actuators since these results are not dependent on any specific type of actuator. Therefore, our $80W$ DC electric motors could equivalently be replaced by any other prime mover with similar torque-speed characteristics and, all other things being equal, the output power numbers would remain unchanged; this would not be true of the input electrical energy which depends on actuator efficiency.

During each experimental run with the monopod, sensor data are logged at a $67Hz$ rate. These stored data are available for later analysis and can be used to extract information regarding the energetic performance of our robot. The instantaneous power output of the motor is simply given by

$$P = \tau\omega \tag{4.1}$$

where τ is the motor torque in Nm and ω the motor speed in rad/s.

This instantaneous power is positive in the first and third quadrants of the motor torque speed curve (Figure 2.2). These are known as the *motoring quadrants* since motor torque and speed are in the same direction and the motor is accelerating. Conversely, in quadrants two and four, known as the *braking quadrants*, the motor torque opposes rotation and the motor slows down. Equation (4.1) yields a negative value of instantaneous output power for operation in the second and fourth quadrants. What is the physical significance of negative power output; what does this braking power cost?

The Galil servo amplifiers used to control the leg and hip motors feature four quadrant, regenerative operation. In addition to controlling the armature current of the DC motor in the motoring quadrants the servo amplifier operates the motor as a generator in quadrants two and four. In these braking quadrants the motor channels regenerated power back to the electrical source. If a battery were used to power the robot, some of this power could be stored and reused later. For now, however, the robot is powered off the grid and the regenerated power is not recovered.

The magnitude of the "free" braking torque is limited and depends upon motor speed and efficiency; any output torque provided in addition to this braking torque draws on the power source. Since it is impossible to determine from the given data what quantity of torque is braking torque and what part draws on the power source, our calculations will assume no regenerated torque. Thus the mechanical power output of the motor is conservatively taken as

$$P = \left\{ \begin{array}{ll} \tau\omega & \text{First quadrant} \\ -(\tau\omega) & \text{Second quadrant} \\ \tau\omega & \text{Third quadrant} \\ -(\tau\omega) & \text{Fourth quadrant} \end{array} \right\} = |\tau\omega|. \tag{4.2}$$

Since the state variable as well as time are available in the logged data, the power given by equation (4.2) can be integrated to give the energy added to the system by each of the motors. The time history of this energy output can also be computed for a given stance phase, flight phase or step. The mechanical energy output of the motor is computed as

$$E_{stance_i}(T) = \int_{t_{td_i}}^{T} P(t)dt\,; \quad T \leq t_{lo_i} \tag{4.3}$$

for the i^{th} stance phase,

$$E_{flight_i}(T) = \int_{t_{lo_i}}^{T} P(t)dt\,; \quad T \leq t_{td_{i+1}} \tag{4.4}$$

for the i^{th} flight phase, and

$$E_{step_i}(T) = \int_{t_{td_i}}^{T} P(t)dt\,; \quad T \leq t_{td_{i+1}} \tag{4.5}$$

for the i^{th} step. Where t_{td_i} and t_{lo_i} are the i^{th} touchdown time and the i^{th} lift-off time, respectively. The mean mechanical power delivered during the i^{th} step can then be computed as

$$\bar{P}_{step_i} = \frac{E_{step_i}}{t_{step_i}} = \frac{E_{step_i}(t_{td_{i+1}})}{t_{td_{i+1}} - t_{td_i}} \tag{4.6}$$

with $E_{step_i}(t_{td_{i+1}})$ given by equation (4.5).

4.3.2 Detailed Energetics

Because of the way the control algorithms are decoupled with vertical motion and pitch control occurring during the stance phase while the foot placement algorithm acts only when the robot is in flight, the energetic cost of each control action is available for individual scrutiny. This allows a unique opportunity, not usually available to experimenters, to examine in detail how energy is used by the robot. Such an analysis can provide valuable insights into where energy is used most effectively and where energy saving strategies could be most successful. Equations (4.3), (4.4), and (4.5) were applied to data obtained during a run with a top speed of $1.2m/s$ to generate the energy output values indicated in Figure 4.5. The seven steps shown represent typical data for steady running.

Since the leg motor acts only to power the vertical motion, the energy involved in controlling the hopping height is given by the dashed curves in Figure 4.5. During the stance phase (top) the energy delivered to the robot by the leg motor increases steadily to a peak value near $13J$ at lift-off. This energy compresses the leg spring to maintain the vertical hopping motion. The dashed curve in the middle field represents the energy involved in backdriving the leg actuator during flight to prepare for the next stance phase. As much energy is used here to backdrive the actuator as to maintain the vertical motion! This is due to the large energy involved in rotating the inertia of the motor plus ball screw at high speed as demanded by the step in actuator setpoint. The energy goes as the square of this inertia. Moreover, the peak power, indicated by the slope of the energy curve, is higher during flight, $P_{flight} \approx 250W$, compared to $P_{stance} \approx 100W$ during stance. Although the power output of the leg motor peaks at a high level during flight, its nominal level is lower, $< 50W$, during most of the flight phase.

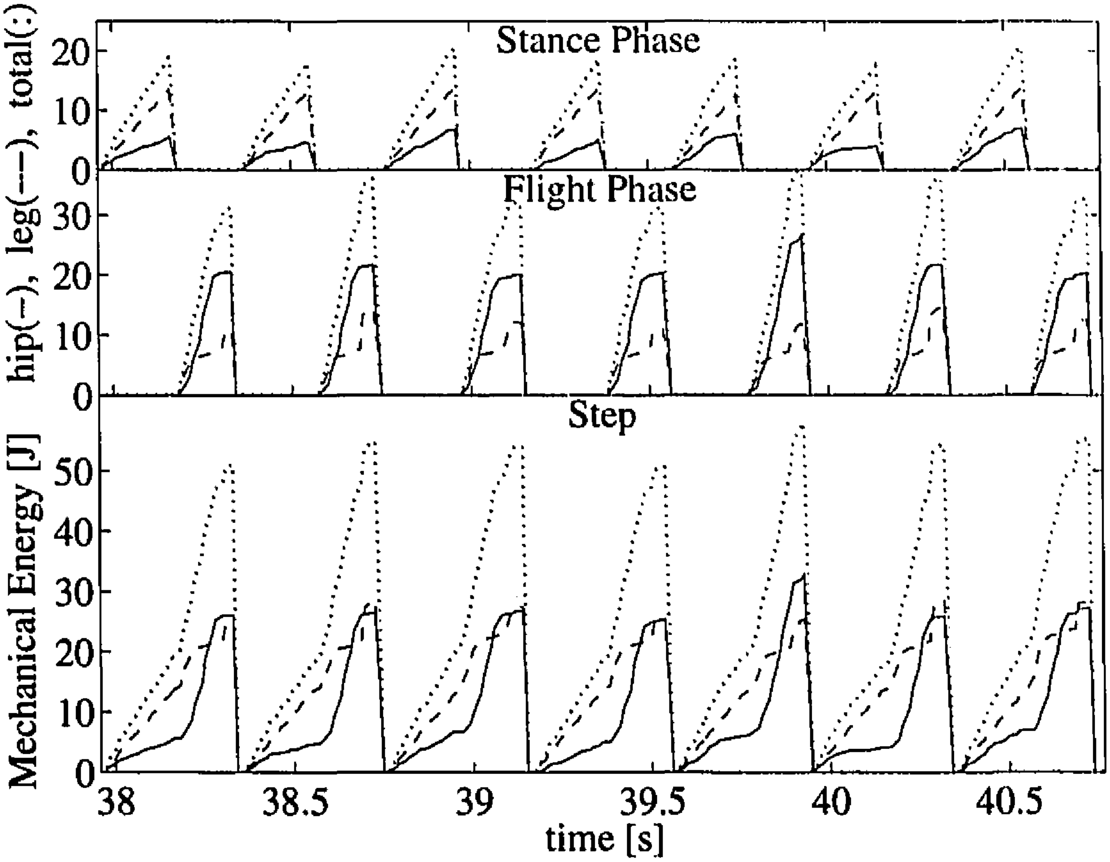

Figure 4.5: *Mechanical energy output of the hip motor and leg motor for running at* $1.2m/s$. *(see Section 4.3.2 for details).*

This behaviour is consistent with a high gain PD controller responding to a step in the position setpoint. The power required is initially high since the velocity of the motor at lift-off is opposite to that desired. The power then levels off as the actuator approaches the setpoint and peaks again when the setpoint is reached and the motor is abruptly stopped.

The bottom field shows energy output for the entire step. Here we see that the leg motor (dashed curve) accounts for approximately half the total energy involved in locomotion at this speed (dotted curve). The energy output of the leg motor during stance depends only on the value of $\bar{\tau}$ in equation (3.1) and on the duration of the stance phase. Although the hopping height controller has no explicit speed dependent term, the stance duration is affected by increasing forward speed which increases the apparent vertical leg spring stiffness [17]. This variation in stance duration links the energy output of the leg actuator to the robot running speed. However, the effect is small compared to the relation between hip motor energy and running speed.

The energy cost of body pitch control is given by the stance phase energy output of the hip motor shown by the solid curve in the upper field of Figure 4.5. Controlling the body pitch accounts for approximately $5J$ at this running speed of $1.2m/s$.

The solid curve in the middle field represents the energy cost of the foot placement algorithm. The energy involved in the FPA is almost twice what is used in backdriving the leg actuator. This is due to the high inertia of the leg which must be driven by the hip actuator. Moreover, the backdriving motion of the leg actuator is assisted by the leg spring which reduces the overall energy requirement for the leg motor. The power output of the hip motor reaches a peak of $\approx 400W$ in the steepest part of the energy curve, then decreases in the flat region of as touchdown approaches. This indicates that most of the actuation happens in the early part of the flight phase.

The lower field shows the equal contribution of each actuator to the total energy cost of locomotion at this speed. While energy is applied steadily during the stance phase, the features of the flight phase energy curves indicate large power fluctuations. Moreover, the contribution of the FPA to overall energy output increases with running speed; already at $1.2m/s$ it is larger than the energy involved in maintaining the hopping height. For this reason, the FPA represents an excellent target for energy minimization strategies. The controller which backdrives the leg actuator is also an appealing candidate for energy reduction since it accounts for such a large portion of the overall energy consumption yet does not directly affect the kinetic or potential energy of the robot.

4.3.3 Mechanical Power Output

The mean mechanical power output of both motors was computed using equation (4.6) for thirteen different experimental runs; a total of 1306 steps. The resulting values of mean power are plotted against running speed in the upper field of Figure 4.6. Each point in the figure represents a single step while the solid line shows the least squares linear fit to the data. The dashed lines suggest upper and lower bounds for mean power output and enclose 98% of the data points.

Looking at the data, two things are immediately evident: mean power increases with running speed, and there is a great deal of scatter to the data. Why does the power increase with speed? The foot placement algorithm increases the leg angle setpoint with increasing running speed. Moreover, a larger setpoint directly affects the energy output of the hip motor since a greater actuator effort is required to track a larger setpoint. This increase in hip energy is reflected in the overall mean power output which includes both motors. At zero speed, the hopping height controller is active and accounts for all the power shown in Figure 4.6. The increase of mean power from $\approx 58W$ at zero running speed to $\approx 125W$ at $1.2m/s$ is almost entirely due to the power output of the hip motor.

The large scatter evident in the data comes from three main sources. First, although power is plotted against average running speed for a given step, this speed may not be constant. At any given time the robot responds to a changing desired speed which is set manually for these experiments. A typical running speed profile shown in Figure 4.4 clearly indicates periods of acceleration (slopes) as well as periods of constant speed (plateaus). Thus power consumption may not be constant since running speed is not constant.

Variations in treadmill speed throughout a given step such as those seen in Figure 4.1 also contribute to fluctuations in mean power. Since the lift-off treadmill speed is used as the speed setpoint for the FPA, variations in the treadmill speed will cause fluctuations in the leg angle setpoint even though the running speed may be constant. Again, this setpoint directly affects the power consumption.

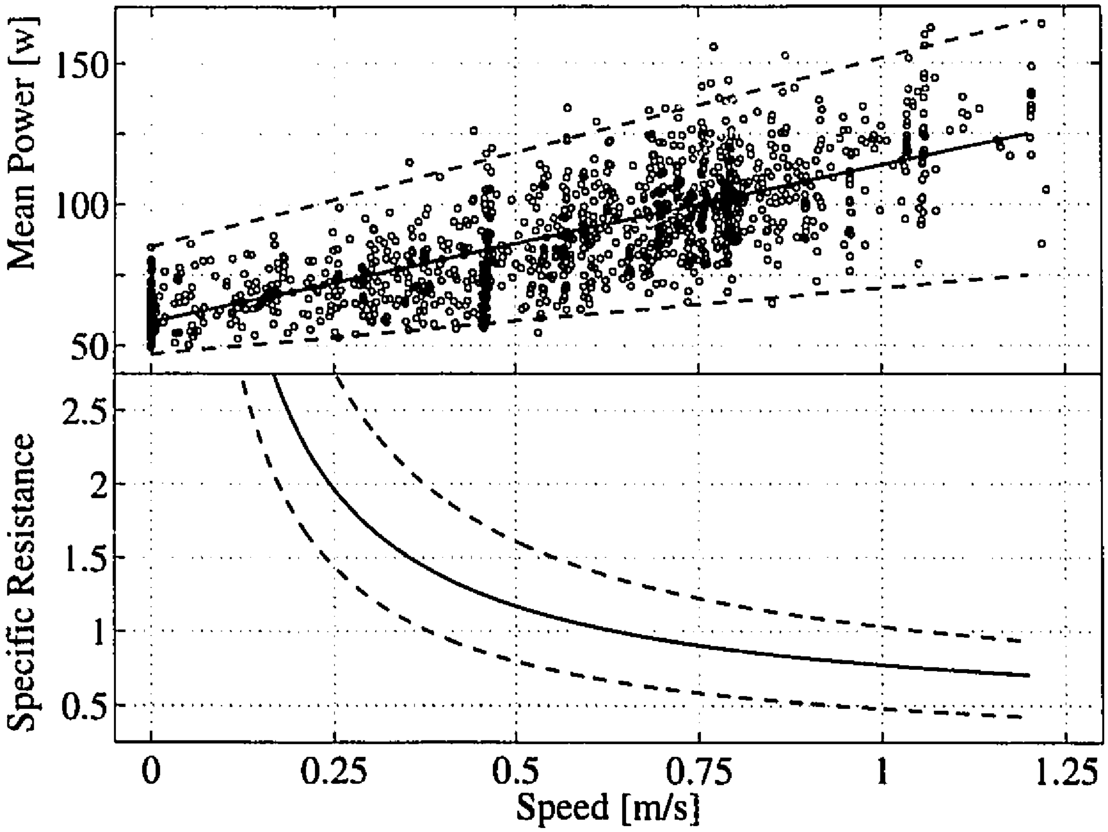

Figure 4.6: *Power Output and Specific Resistance. The upper field shows total power output of the motors at various speeds. Each data point represents one step; the solid line represents an average and the broken lines enclose 98% of the data points. The lower field shows specific resistance vs. robot speed computed from the same data.*

Third, even at constant running speed, the robot position fluctuates about the centre of the treadmill. An integral term is included in the FPA to keep the robot from moving too far from the treadmill centre. This integral term reflects fluctuations in robot position onto the leg angle setpoint thereby affecting mean power.

4.3.4 Specific Resistance (ε)

In order to get a full evaluation of the energetic performance of the ARL Monopod, the cost of locomotion for our machine should be compared to that of other similar machines. However, power output taken in isolation does not tell the entire story. A fair comparison must consider not only the cost of locomotion in terms of output power but also the performance achieved in terms of the mass moved and the velocity attained.

In 1950 Gabrielli and von Kármán suggested that a non-dimensional parameter, *specific resistance*, ε, defined as the ratio of power output, P, to the product of maximum speed, v_{max}, and vehicle weight mg;

$$\varepsilon = \frac{P}{mgv_{max}}$$

could be used to compare all vehicles regardless of size, speed or configuration. In this way, the parameter encompasses the cost of locomotion as well as the performance achieved. By plotting ε against speed they successfully compared the energetic performance of land, air and sea vehicles as well as biological systems on the same scale [10].

Gabrielli and von Kármán originally defined ε using v_{max} to extract a single number for the specific resistance. This simplified the collection and presentation of data and brought their enormous task of comparing a large number of different vehicles into the realm of the possible. When energetic performance data is available as a function of speed as is the case for our robot, one can equivalently compute specific resistance as a function of velocity

$$\varepsilon(v) = \frac{P}{mgv} \tag{4.7}$$

where $\varepsilon = \varepsilon(v_{max})$ by the original definition.

Since no mechanical work is performed by moving a mass horizontally at a constant speed, many authors use specific resistance as a measure of energetic efficiency for vehicles. The name specific resistance comes from an interpretation of ε as measure of the resistance to motion offered by the medium in which the motion occurs. Since the output power of the prime mover is used in defining ε, the resistance referred to includes not only external effects such as aerodynamic drag or rough terrain conditions, but also considers the resistance to motion caused by transmission losses. Of course a more useful measure of energetic performance would consider the load carrying capacity of the vehicle but such data is not always available. Moreover, in the field of dynamically stable legged locomotion the goal is still to stabilize the running motion of the vehicle without any extra cargo.

Using equation (4.7), the power output data in the upper field of Figure 4.6 are presented in the lower field as specific resistance vs. running speed. Even though the mean power increases with running speed, ε decreases as the speed goes up. Similarly, the dashed border lines diverge in the mean power plot but seem to converge in the specific resistance plot indicating that fluctuations in power cost have a smaller effect on ε at higher running speed.

The decrease of ε with speed suggests that the robot uses energy more efficiently the faster it runs. This trend can be understood by considering the power used to maintain the vertical motion. This power is insensitive to running speed compared to the hip motor output power and although necessary to the running motion, it can be considered as a type of "overhead cost" which exists even when the speed is zero. At zero speed, the performance is zero so any finite power output causes the specific resistance to blow up. As the running speed increases, the power cost also increases but the change is small compared to the overall power output so that ε decreases. At $1.2m/s$ the leg motor power accounts for half the overall power cost and the specific resistance reaches its lowest value of $\varepsilon = 0.7$. The low-speed value of ε may decrease by specifying a hopping height setpoint which varies as a function of forward speed; this would lower the power cost of the leg motor for slower running. The hopping

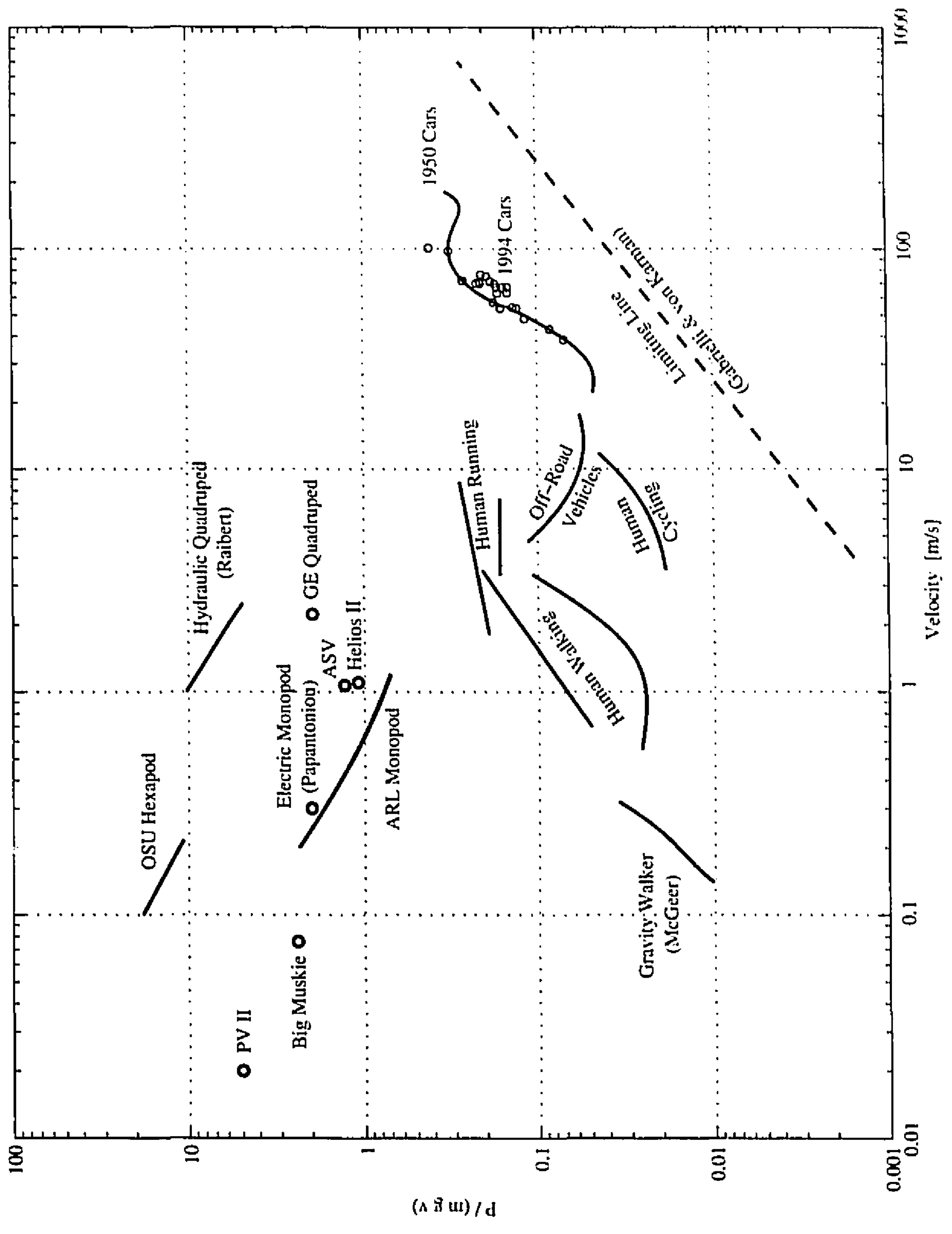

Figure 4.7: *Specific Resistance for selected land vehicles (see Section 4.3.4 for details).*

height was kept constant in these experiments to maintain a steady step duration.

Figure 4.7 presents the specific resistance of selected land vehicles on a log-log scale. Some of today's legged machines (static walkers as well as dynamic walkers) appear prominently in the upper left hand corner far from the Gabrielli and von Kármán limiting line (GvK line). The GvK line was proposed as a practical limit to vehicle performance based on 1950 data. Wheeled vehicles appear just above the GvK line and ε values for human locomotion appear to the left of wheeled vehicles.

It is important to realize when considering the figure that while we have taken every effort to accumulate the most accurate data possible for each vehicle, the results are still not clear cut. The difficulty arises from the inability of ε to account for the different methods of computing output power for each different type of vehicle. For automobiles, the quoted maximum power does not usually correspond to operation at maximum speed but rather at maximum acceleration. Some of the other vehicles have short term power storage devices such as a hydraulic accumulator or a flywheel which lower the mean power consumption while supplying peak power requirements. Moreover, conventional vehicles carry their power sources on board while most legged machines do not. There is a great advantage to not having to move the extra mass of a power source at top speed. Also, the additional mass of this power source is not included in the vehicle mass and is not revealed by the value of ε. Many vehicles have parasitic power losses which do not contribute directly to locomotion but drain the available power and increase ε.

All these issues conspire to reduce the quantitative analysis portrayed in Figure 4.7 to something more qualitative. In short, while the values of ε have been computed from the best available data, ε does not tell the entire energetic story; one should be wary of drawing sweeping conclusions from the data. Having said this, specific resistance remains a standard parameter for comparing energetic performance and is used by many authors to evaluate the performance of legged vehicles.

Legged Machines

Beginning in the top left and moving across, the following legged machines are included in Figure 4.7. Points are used where only maximum speed data are available; curves represent specific resistance as a function of speed for the given machine.

- PV II built by Hirose[13] is a $10kg$ quadruped whose leg design is based on a pantograph mechanism which simplifies the kinematics of locomotion.
- Big Muskie [8] is a $12\,200\,000kg$ coal mining dragline. At the time of its construction it boasted the world's longest electric extension cord.
- The OSU Hexapod [9] is $130kg$, six-legged static walker. Power from the grid is channeled to 18 electric drill motors which actuate each of the three joints per leg through a wormgear transmission.
- Papantoniou [24] built an electrically actuated monopod which uses a gait termed "compliant walk" to move in the plane. His externally powered machine achieved a top speed of $0.3m/s$.
- The Active Suspension Vehicle (ASV) [26] was built at Ohio State University after the OSU hexapod. The six-legged ASV is a $2700kg$ power autonomous static walker capable of moving over rough terrain and carrying a $230kg$ pay load. It carries an operator but is also capable of self-guided locomotion.
- Helios II [3], built by Hirose, is a tracked vehicle with four independently articulated and controlled tracks.
- The GE Quadruped [21] was built in 1968 by General Electric Corporation. This $1350kg$ hydraulic mechanism relied entirely on an operator to control each of its limbs and used a force feedback system to reflect motions of the operator's arms and legs into movement of the machine's limbs.

- Raibert's hydraulic quadruped [32] weighs $25kg$ and is capable of locomotion using any of a number of gaits including *trotting*, *pacing*, and *bounding*. Raibert's machines were constructed to investigate design and control issues for robotic locomotion and not to be power autonomous. Nevertheless, his quadruped is included in the figure for the sake of completeness.

- McGeer's gravity walker [16] appears on the figure as much as three orders of magnitude below the other legged machines. This $3.5kg$ mechanism was constructed to investigate the similarity between the walking motion of legs and the rolling action of wheels. His unpowered system moves down an inclined plane using gravity to drive its motion. The similarity between the motion of the gravity walker and a single wheel explain its specific resistance value which has more in common with that of wheeled systems than of legged machines.

We have also included the ε values for our electric monopod from Figure 4.6 on this figure (labelled ARL Monopod). Notwithstanding McGeer's device which is unpowered, our robot currently has the lowest specific resistance among the legged vehicles surveyed with $\varepsilon = 0.7@1.2m/s$.

Human Locomotion

Although legged machines are studied as an alternative to wheeled systems, it is instructive to compare machine locomotion with human locomotion. Figure 4.7 includes five curves for human walking, running and cycling. Data are collected for different subjects. The curves presented here represent an average of the data used.

- The upper curves for walking and running are from Cavagna [6]. Cavagna used cinematography to record movements of the arms and legs in walking and running. from the positions of the limbs measured in each frame, velocity and acceleration data were deduced. Together with estimates of mass and inertial properties of the limbs these data were used to derive potential energy and kinetic energy for each limb. These energies, in turn yielded output power for the locomotion.

- The lower curves for walking and running are taken from Margaria [14]. Margaria used force plate records to obtain foot impact force histories for walking and running. These forces were used to derive horizontal and vertical components of acceleration during contact. These accelerations are integrated to give kinetic and potential energy values.
- The data for human cycling is from Pugh [25]. Pugh used a bicycle ergometer which measures power at the pedals to compute power output of the muscles for cycling at various speeds.

It is noteworthy that the cycling data for ε relates more closely to that for cars than for humans. This confirms that the type of motion is more important than the power source in determining the specific resistance and implies that for each type of locomotion there is an optimal performance regardless of the type of prime mover.

Wheeled Machines

Since legged machines are proposed as an alternative to conventional wheeled vehicles, their performance must be compared against these vehicles. For wheeled vehicles, lines correspond to a fit through data for different vehicles of the same class. The points represent specific resistance values of single vehicles.

- The data labelled 'off-road vehicles' is taken from Bekker [4]. Although the specific resistance of off-road vehicles is more in line with legged systems at low speeds, it converges with that for automobiles as velocity increases. It is important to consider conventional off-road vehicles since rugged terrain, now the domain of wheeled and tracked systems, represents the most likely proving ground for practical legged machines.

- The curve labelled '1950 Cars' is taken from the Gabrielli and von Kármán study. They are included here as the classic data and are compared with contemporary cars. The high speed section of this curve was labelled 'race cars' in the original study; no distinction is drawn here.

- The data points labelled '1994 Cars' were calculated from specifications published by selected auto manufacturers. Source data for the individual cars is given in Table 4.1.

It surprising at first to see such good agreement between today's high performance, sophisticated automobiles and those produced 44 years earlier. However, it is important to note that the original curve represents the borderline of *best possible performance* for cars of the day. Almost all the 1994 cars surveyed lie either directly on or slightly below this curve. Another misleading factor is that the maximum speed attained does not generally correspond to the maximum power output. This fact was discussed by Gabrielli and von Kármán who also used manufacturer's data. While today's cars have lightweight chassis and engine components compared to 1950 cars, these lighter engines generally produce more power. Higher power output and lighter mass conspire to increase the value of ε for a given top speed.

Legged vehicles generally have a long way to go before they successfully compete with conventional off-road vehicles or biological systems on the basis of specific resistance. Nevertheless, we have shown that dynamically stable legged locomotion is possible on a tight energy budget. Work aimed directly at improving energy efficiency of these machines should continue to narrow the gap.

Manufacturer	*Model*	v_{max} [km/hr]	*Curb Weight* [kg]	*Engine Power* [kW]	ε
BMW	M3	249	1460	213	0.210
	325is	206	1400	141	0.176
Dodge	Viper RT10	257	1581	298	0.264
Ford	Probe	227	1316	122	0.147
Honda	Civic del Sol	193	1087	93	0.160
Lexus	GS 300	240	1665	163	0.147
	LS 400	240	1780	186	0.157
	SC 400	240	1645	186	0.169
Maclaren	F1	362	1138	474	0.414
Mazda	RX-7	254	1270	190	0.211
Pontiac	Firebird	256	1566	205	0.184
Porsche	911	270	1390	201	0.193
	928 GTS	275	1630	257	0.207
	968	251	1470	176	0.173
Toyota	MR2	249	1565	238	0.220
Vector	W8T Turbo	351	1506	466	0.317
Volkswagen	Corrado VR6	225	1274	133	0.167
	Eurovan	155	2240	81	0.084
	Eurovan Diesel	139	2140	57	0.070
	Golf Cl	173	1176	66	0.117
	Golf GTI	195	1143	85	0.137
	Jetta GL	193	1217	85	0.130

Table 4.1: *Source data for ε values of 1994 automobiles*

Chapter 5

Energy Conservation Strategies

Notwithstanding the encouraging results already attained with the ARL Monopod, we are confident the energetic performance of the machine can be further improved. The experimental results as well as the energetic analysis of Chapter 4 have provided insights into the detailed operation of the robot which suggest methods for reducing the overall energy cost. The implementation of new control ideas and appropriate hardware modifications should go a long way towards reducing the energy requirements for stable running. Some of the strategies discussed in this chapter have been implemented to some degree while others have been simulated or studied as theoretical exercises. Still, we feel that, once implemented, these ideas could reduce the energy cost of robot locomotion.

5.1 Novel Control Ideas

The control algorithms discussed in Chapter 3 were designed solely to stabilize the running motion of the robot without regard to the energy expenditure for actuation. As discussed in Section 4.3.2, the simple PD laws used for flight phase control present the greatest opportunity for energy conservation. Novel control laws aimed at tracking the desired touchdown setpoint but sensitive to energy output of the actuators could replace the conventional PD controllers which are insensitive to energy output.

5.1.1 Locomotion Time (ϵ)

The controllers discussed so far operate in the absence of knowledge regarding the duration of an upcoming stance or flight phase. This forces the controllers to be reactive and depend on state switching triggers, lift-off and touchdown, to initiate action. For example, if a certain touchdown position is desired, the actuator must move quickly to that position at the onset of the flight phase since the controller has no knowledge of when touchdown will occur. Thus the control algorithm must specify a flight phase setpoint and hope the actuator reacts quickly enough to track the position before the robot touches down.

A better approach would involve metering action depending on the expected time available to attain the goal. In this way, knowledge of the time available allows allows a controller to specify not only a setpoint, but also a desired path that reaches this setpoint at any desired instant.

Buehler et al. [5] developed a "phase angle" variable which maps the unknown, varying time interval involved in ballistic flight onto a known, fixed interval. This variable proved critical for the stable coordinated control of the "two-juggle," a robotic juggling task with two pucks. This same measure, given here as the locomotion time,

$$\epsilon \triangleq \frac{\dot{z}}{\sqrt{2g(z - z^*) + \dot{z}^2}}, \tag{5.1}$$

can be used to map the unknown duration of the flight phase onto a known interval. For vertical hopping, with the touchdown and lift-off position at z^* the locomotion time of equation (5.1) maps a flight (or stance) phase onto the interval $(-1, 1)$ between lift-off and touchdown, with $\epsilon = 0$ at apex (max. compression). Moreover, if we assume zero dissipation during flight phase, its derivative, $\dot{\epsilon}$, is constant. Essentially, ϵ compresses or expands the flight duration to fit between the limits $(-1, 1)$ while keeping the flow of time constant.

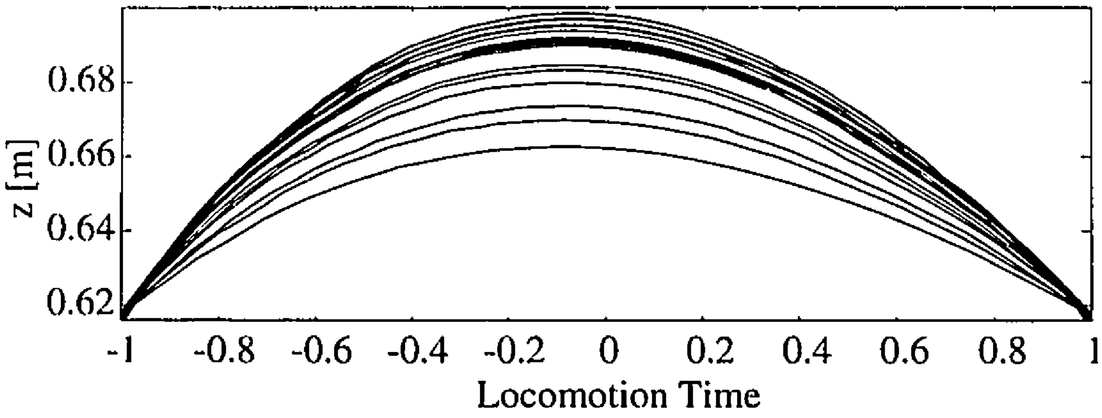

Figure 5.1: *Locomotion Time (ϵ) vs. body height (z) for vertical hopping. The value of ϵ is calculated online during an experimental run using equation (5.1). Despite changing hopping height, flight duration is constant in the epsilon domain. Moreover, the ballistic flight path remains parabolic when plotted against ϵ.*

Figure 5.1 shows the locomotion time computed online for an experimental run. Although the flight duration varies with changing hopping height, when plotted against the locomotion time, the curve clearly shows lift-off at $\epsilon = -1$ and touchdown at $\epsilon = 1$. By planning controller action based on the locomotion time, any path can easily be mapped onto real time.

Trajectory Tracking

The foot placement algorithm of equation (3.2) specifies a touchdown toe position, x_f, which stabilizes the running motion. Thus, any trajectory for the toe which contains the point (x_f, t_{td}) will successfully stabilize robot running. When the flight duration is unknown, the only implementable trajectory which stabilizes the motion is a step of amplitude x_f. However, using the locomotion time, ϵ, the instant of touchdown is known and a path can be chosen which additionally matches the lift-off and touchdown speed of the toe to the running speed, $\dot{x}_f = \dot{x}_{lo} = \dot{x}_{TM}$. This "ground speed matching" eliminates high accelerations at lift-off and high impact loads at touchdown resulting in a reduced peak actuator power, smoother swinging motion of the leg and less wear on the system.

Figure 5.2 shows experimental leg angle data for two successive steps at $0.7 m/s$ running speed. The solid curve shows the actual path followed by leg which swings at an approximately constant rate during stance and responds to a step in position setpoint during flight. The flight phase leg angle is tracked using a high gain PD control law.

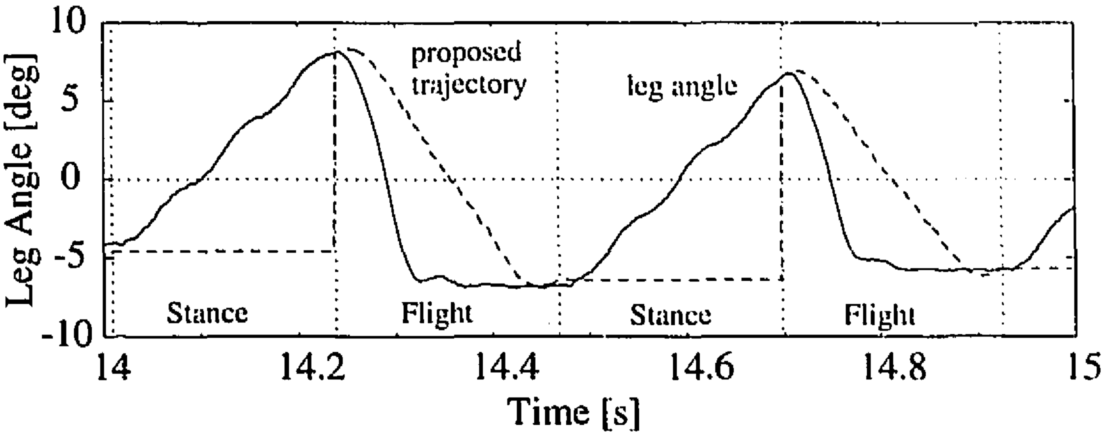

Figure 5.2: *Actual leg swing and proposed reference trajectory. The solid curve shows the cyclic swinging motion of the robot leg about the vertical position, zero leg angle, for running at 0.7 m/s. During the flight phase the leg angle is servoed to a desired touchdown value that will assure stable running. The broken line indicates the proposed reference trajectory. This trajectory implements ground speed matching by matching the leg swing rates at lift-off and touchdown to the treadmill speed.*

The dashed curve in Figure 5.2 shows a proposed reference trajectory which is computed online using ϵ. This reference trajectory is formed by a parabolic curve at lift-off, a tangent line and a second parabolic curve at touchdown and is given by

$$\theta = \begin{cases} \theta_{lo} + \frac{\dot{\theta}_{lo}}{\dot{\epsilon}}(\epsilon + 1) + \frac{\ddot{\theta}_{lo}}{2\dot{\epsilon}^2}(\epsilon^2 + 2\epsilon + 1) & , \quad -1 \leq \epsilon \leq \epsilon_1 \\ \alpha_0 + \alpha_1 \epsilon & , \quad \epsilon_1 < \epsilon \leq \epsilon_2 \\ \theta_{td} + \frac{\dot{\theta}_{td}}{\dot{\epsilon}}(\epsilon - 1) + \frac{\ddot{\theta}_{td}}{2\dot{\epsilon}^2}(\epsilon^2 - 2\epsilon + 1) & , \quad \epsilon_2 < \epsilon \leq 1 \end{cases} \tag{5.2}$$

where θ_{lo} and $\dot{\theta}_{lo}$ are the actual lift-off leg angle and rate, θ_{td} is the touchdown angle specified by the FPA, and $\dot{\theta}_{td}$ is the touchdown swing rate which matches the ground speed. In addition, the trajectory specifies $\ddot{\theta}_{lo}$ and $\ddot{\theta}_{td}$, which are, respectively, the lift-off and touchdown angular accelerations of the leg and relate to the motor torque. a_0 and a_1 in equation (5.2) define the line which is tangent to both parabolic paths and depend on the initial and target conditions. c_1 and c_2 are the tangency points between the line and the first and second parabolas, respectively. This reference trajectory matches lift-off and touchdown leg swing rates to the stance phase leg swinging and corresponds to a constant-magnitude actuator torque in the parabolic region if the motion is frictionless. Although both the reference trajectory and the setpoint include the same touchdown leg angle, the reference trajectory additionally matches the rates as well as distributing actuator effort throughout the entire flight phase in theory lowering overall power requirements.

Equation (4.3) was used to compute the flight phase energy output of the hip motor for six successive steps at $0.8m/s$ running speed. The results presented in Figure 5.3 are from two separate experimental runs. In the upper field, the flight phase leg angle is responding to a step in position setpoint. Below, the leg angle is following the reference trajectory defined above. Notwithstanding the step-to-step fluctuations in overall energy output which are discussed in Section 4.3.3 the difference in shape and magnitude of the energy output for each run is immediately obvious. When the setpoint is used, the energy shoots up rapidly as the step is applied then levels off for the remainder of the flight phase while the leg holds position. This behaviour is seen in the actual leg angle curve of Figure 5.2. The lower field shows that when the reference trajectory is used, however, the energy generally increases more steadily throughout the entire flight phase in response to a trajectory that also changes smoothly. The difference in overall energy for these two runs is also apparent.

The mean power data from the upper field of Figure 4.6 are shown again in Figure 5.4. In this figure the data have split; values in the upper field are from experiments

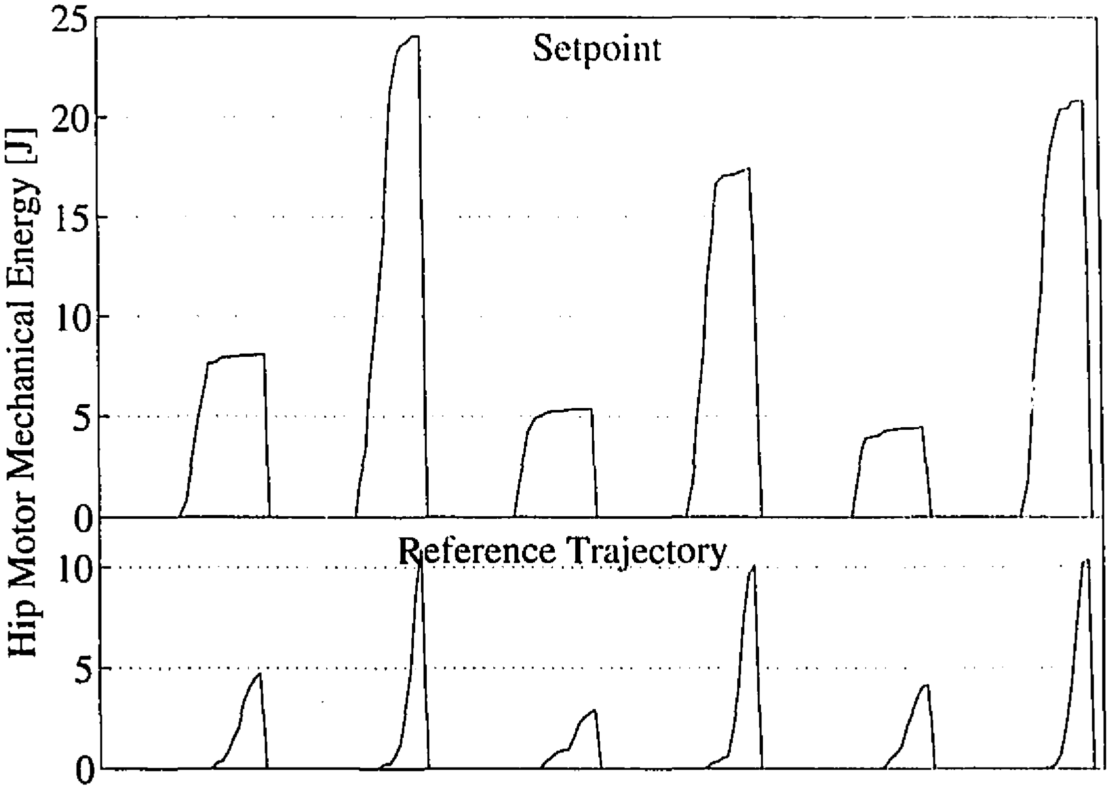

Figure 5.3: *Hip Motor Mechanical Energy. The energy delivered to the system during flight by the hip motor is shown for six successive steps. The upper curve depicts a run where the flight phase leg angle tracked the setpoint computed by the foot placement algorithm. In the lower curve, the leg angle followed a reference trajectory based on the locomotion time variable. This trajectory terminates at the setpoint specified by the FPA. The running speed was* 0.8m/s *in each case.*

in which the conventional step was used for flight phase leg angle control. The lower field shows mean power when the reference trajectory described above is implemented. There are 702 steps represented in the upper field, 604 below. As before, the lines represent the least squares linear fit to the data. Despite the obvious difference in energy consumption for the six steps shown in Figure 5.3, when the data from various runs are taken together there is no difference in overall power cost! In fact, despite the scatter evident in the data, the average power represented by the linear fit for each data set varies by less than 1% over the entire speed range.

Why is there no power saving? There are two possible causes. First, the reference trajectory technique may not be as successful as hoped because it attempts to do too much. In addition to matching the touchdown leg angle, the rate is also matched. This is a tricky thing to do since any error in timing, perhaps due to poor sensitivity on the state switch, could cause the touchdown position to vary significantly from the desired position which could cause over correction on subsequent steps. This is not the case with the setpoint controller since the touchdown rate is fixed so variation in the exact instant of touchdown does not affect touchdown position. Moreover, in order to match the treadmill speed, the leg is swinging at touchdown rather than holding a constant position as it does with a simple step in leg angle setpoint. The extra energy associated with this non-zero swinging speed could account for extra energy. The second possible cause for the missing power saving has to do with the PD controller which is used to track both the setpoint and the reference trajectory. This is discussed below in Section 5.1.1.

Although the reference trajectory technique was not successful in reducing the flight phase hip motor power, the technique could be adapted for ball screw backdriving where it may prove more successful.

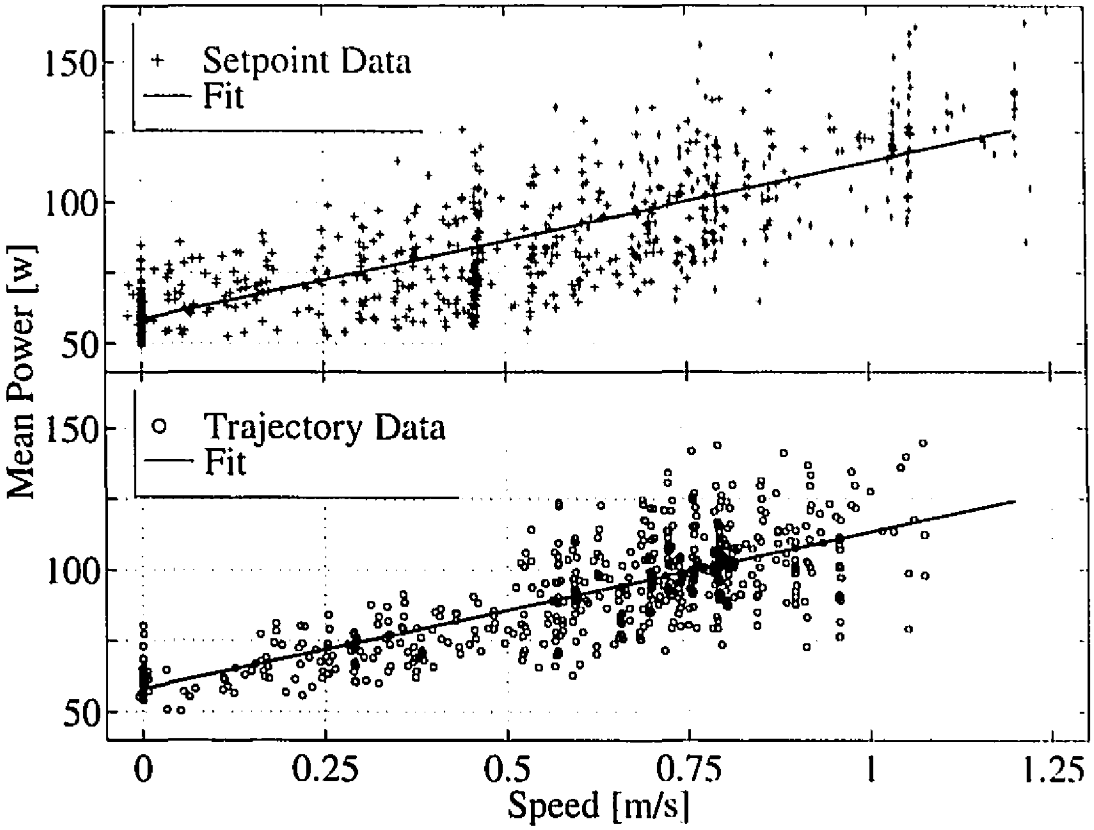

Figure 5.4: *Mean Mechanical Power (both motors) vs. Running Speed reproduced from Figure 4.6. Each data point represents a single step, the lines show the least squares fit to the data. Data in the upper field are taken from six experimental runs in which the flight phase leg angle responds to a setpoint. The lower field shows data from seven experimental runs where the flight phase leg angle tracks to a reference trajectory computed using the locomotion time variable.*

PD Controller with Epsilon-Dependent Gains

Even when a reference trajectory is specified for the desired flight phase leg angle instead of a step, a PD controller is employed to ensure the actual leg angle tracks to this reference trajectory. Indeed, since rate as well as position are to be matched at touchdown, tracking accuracy becomes even more crucial. For this reason, the PD gains must be kept high. This drives the hip motor torque to elevated levels whenever the leg angle diverges from the reference trajectory. Moreover, the high gains amplify sensor noise which shows up as high frequency, large amplitude spikes on the motor torque signal. Such disturbance torques add to the energy output of the motor reducing overall efficiency for locomotion.

A closer examination of the problem reveals that tracking of both leg position and rate are assured at lift-off since the reference trajectory is computed according to these data. The linear portion of the trajectory only suggests how the leg angle may approach the touchdown setpoint and so tracking requirements are not stringent in this region either. In fact, tracking accuracy only becomes important in the latter part of the flight phase as the robot approaches touchdown.

Thus tracking accuracy requirements, which relate to the values of the PD controller gains, vary throughout the flight phase. By specifying controller gains as a function of the locomotion time, torques could be kept at relatively low levels by having lower controller gains at $\epsilon = -1$ while tracking accuracy is assured where needed by increasing the gains as ϵ approaches the touchdown value of $+1$.

5.1.2 Robust Control Theory Approach

In addition to constructing the ARL Monopod, a dynamical model and computer simulation were developed based on the physical device. This work was primarily carried out by M. Ahmadi who was able to validate his model and simulation against experimental data obtained with the physical device. The existence of such a model which accurately predicts robot behaviour enables the development of advanced, model-based controllers for locomotion.

A method of synthesis exists in the field of Robust Control Theory which can be used to design a stabilizing controller representing the optimal solution to a given control problem posed in the frequency domain. For our application the problem could be posed in terms of a *Mixed Sensitivity Minimization* in which a stabilizing feedback controller is sought which tracks a reference leg angle in light of sensor noise and simultaneously minimizes the H^∞ norm of the input torque signal. A complete problem description includes frequency dependent weighting functions which define acceptable tracking errors and expected sensor noise spectra, as well as accounting for the range of angle setpoints and acceptable torque signals.

Initial attempts have been made to design such a controller based on a simplified model of robot dynamics which would replace the PD controller for flight phase leg angle tracking. The design procedure requires a solid background in frequency response techniques as well as a great deal of patience. Although our attempts did furnish a controller which proved to be sensitive to input torque and actuator bandwidth, simulation of this controller also revealed the tracking performance to be much less than adequate. Further research into this area could, however, ultimately yield positive results and work should not be abandoned.

5.1.3 State Space Techniques

The dynamical model described above in Section 5.1.2 can also be used as the basis for model-based controllers designed in the time domain. A technique for *Minimum-Energy Control* is described by Chen [7] which could be adapted for flight phase leg angle control. This technique minimizes the L^2 norm of the input torque, $\|\tau(t)\|_{L^2}$, while driving the system from the initial state $(t_{lo}, \theta_{lo}, \dot{\theta}_{lo})$ to the final state $(t_{td}, \theta_{td}, \dot{\theta}_{td})$, where t is time, θ is the hip angle and $\dot{\theta}$ the angular rate.

Applying this design method to a simplified model of the robot described only by a leg inertia I and a hip torque τ, we obtain a feedback law which returns the minimum-energy torque as a function of time

$$\tau_{min}(t) = \frac{2t}{(t_{td}-t)^2}\left(3(\theta_{td}-\theta(t)) - (t_{td}-t)\dot{\theta}_{td} - 2(t_{td}-t)\dot{\theta}(t)\right). \qquad (5.3)$$

Notice that equation (5.3) does not explicitly refer to the lift-off state but rather depends only on the current and final states. Thus the control law is memoryless and can easily be implemented as a real-time controller.

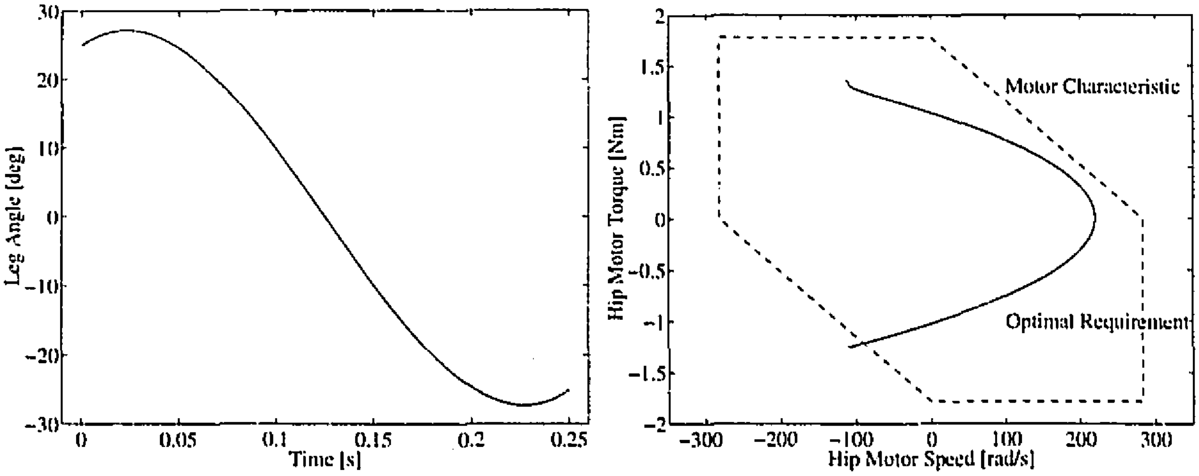

Figure 5.5: *Minimum Energy Control: Trajectory Followed (left) and Torque Requirement (right)*

Simulating this controller for the simplified system we obtain the results shown in Figure 5.5. The simulated leg angle is shown on the left. There is no concept here of a reference trajectory, rather this is the simulated, "actual" path followed by the leg in response to the torque generated by the control law of equation (5.3). On the right side of Figure 5.5 we show the hip torque which has been scaled down by a factor of 30, equal to the actual hip transmission ratio. This allows the torque speed curve of our Maxon motor taken from Figure 2.2 to be plotted on the same field (dashed curve). Even though the legs swings through 50° in 0.25s, the required torque lies well within the motor characteristic curve everywhere except at lift-off.

Although the controller is termed "Minimum Energy" this refers to the spectral energy of the input torque signal and is not explicitly related to the actuator energy output. What is the physical significance of minimizing $\|\tau(t)\|_{L^2}$? Consider the simplified model for a DC motor given in Figure 5.6 consisting of a constant winding resistance R_a, an input voltage V, and a back EMF $E_g = K_e\dot{\theta}$ where K_e is the electrical constant of the motor and $\dot{\theta}$ is the motor speed. Neglecting the effect of the winding inductance, the torque output of the motor is given by $\tau = K_m i_a$ where K_m is the mechanical constant of the motor, and the current through the rotor winding is given by $i_a = (V - E_g)/R_a$. The power dissipation across the rotor winding is now given by

$$P_{loss} = V_{R_a} i_a = i_a{}^2 R_a$$

and the corresponding energy loss is

$$E_{loss} = \int P_{loss} dt = \int i_a{}^2 R_a\, dt = \frac{R_a}{K_m^2}\int \tau^2 dt = \frac{R}{K_m^2}\sqrt{\|\tau(t)\|_{L^2}}.$$

Thus the minimum energy controller actually minimizes energy dissipated as heat through the motor armature. Although minimizing this quantity would not affect the specific resistance, it would reduce the electrical power consumption of our robot. This is an important goal since at stall torque our $80W$ motors can dissipate as $\approx 400W$ of heat through the armature winding. This power level can only be maintained for a brief period limited by the thermal time constant of the motor.

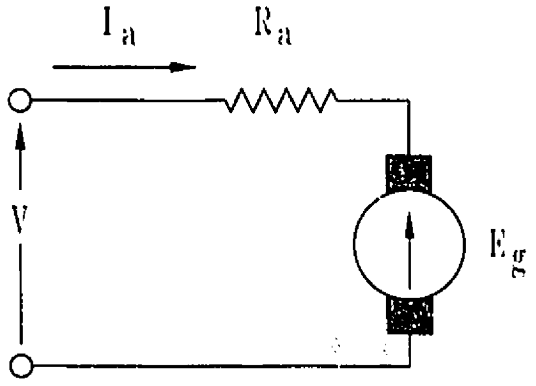

Figure 5.6: *Static Electric Circuit Model of a DC Motor*

This type of model-based controller which depends on an accurate state-space description of the system is very sensitive to modelling errors and unmodelled dynamics.

This means that a simple feedback law such as that given by equation (5.3) may not exist in a practical, implementable form for the ARL Monopod. Moreover, the controller would not respond to changing system parameters. Even so, such a controller based on a more complete dynamical model could be simulated to yield a "minimum-energy reference trajectory" similar to the trajectory shown in Figure 5.5. Such a trajectory would have to be scaled according to the actual lift-off state and the target touchdown state given by the FPA, and the locomotion time would be used instead of the real time. The resulting trajectory could replace the piecewise reference trajectory discussed in Section 5.1.1.

5.2 Hardware Modifications

5.2.1 Compliant Hip Actuation

During flight, the hip motor has to decelerate sharply, accelerate and then decelerate the leg, which requires peak power of our motors at top running speed. Most of this return swing motion of the leg could be provided by a properly dimensioned spring in series with the hip actuator. This has been proposed and experimentally tested in passive (unstable) mode by Raibert [31].

Our robot has been designed to accommodate such springs as part of the hip actuation system. The equations of Section 2.2.2 were developed taking into account this compliance. Equation (2.5) gives the motor torque required to swing the leg through a sinusoidal path. A large value was used for the hip compliance, k_h, to simulate direct actuation for selection of the transmission parameters. The same equation can also be used to determine the torque speed requirements for compliant actuation of the hip joint. Figure 5.7 shows the hip motor torque requirements for both types of motion plotted against motor speed. The dotted curve represents the motor limit while the circular dashed curve shows the requirement for direct actuation. Although direct actuation of the 25° sinusoidal path is easily accommodated by the motor, the

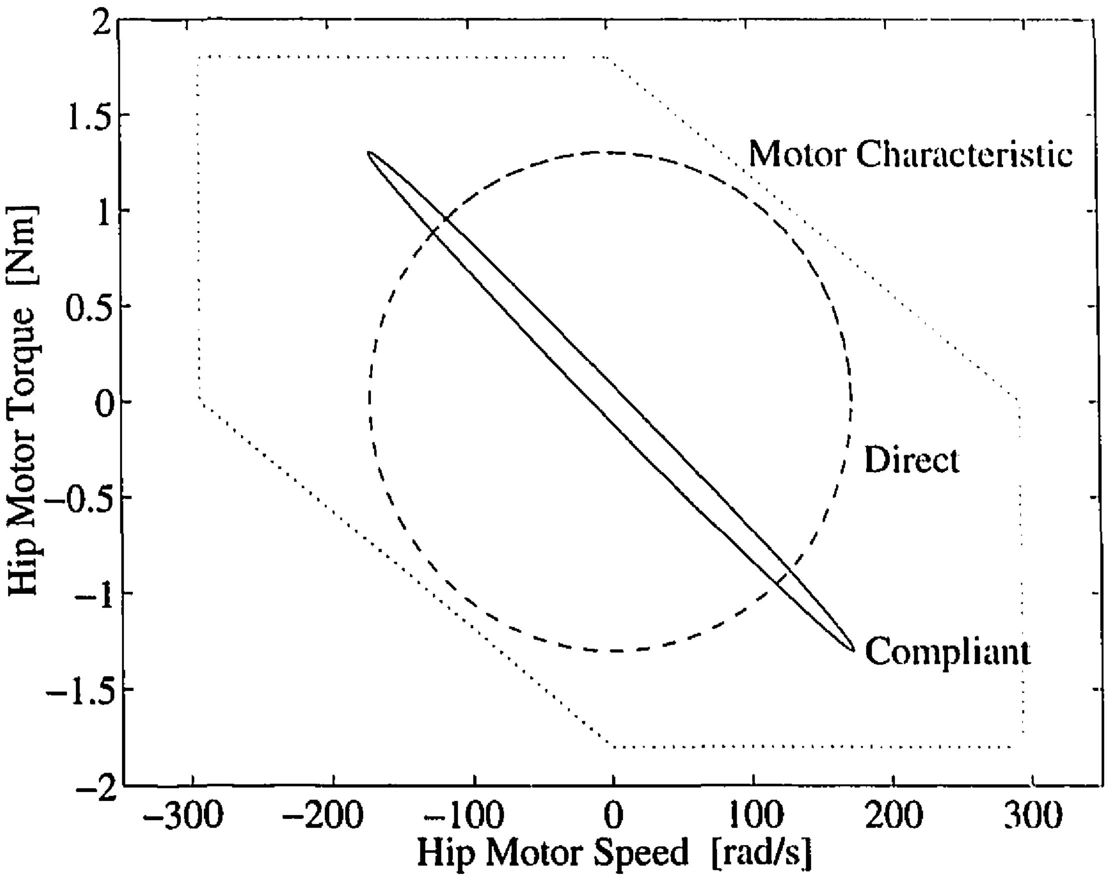

Figure 5.7: *Active Hip vs. Passive Hip. The figure shows simulated hip motor torque speed requirements to follow a 25° sinusoidal reference trajectory for leg angle. The dotted curve shows the motor operating range from Figure 2.2. The dashed curve shows the requirement using direct actuation where the motor alone powers the motion. The solid curve represents the requirement for a passive hip where the bulk of the motion is powered by energy stored in a hip compliance and the motor merely makes up for losses.*

requirement is greatly reduced when the compliance is added (narrow, solid curve).

We have developed a controller which stabilizes the passive dynamic mode of robot running in simulation based on a simplified dynamic model of the physical robot. The next step involves adapting these control concepts to stabilize the more complete simulation which has been validated against experimental runs with the robot. This work, performed by M. Ahmadi, represents an important first step towards implementing passive dynamics in experiment. We are currently evaluating the suitability of commercially available latex tubing which we hope to use for the hip compliance on the robot.

Compliant Running and Torsional Spring Design

In conjunction with attempts to implement passive dynamic running on our prismatic, planar robot, a second robot, the Compliant Articulated Robotic Leg (CARL) has been constructed at ARL [18]. The design of CARL's actuation systems is based on simulation work in which compliant elements are included in series with both the knee and hip actuation systems. Moreover, CARL contains a passive, revolute ankle which has a compliance but no actuator. Since all of CARL's joints are revolute, we have been developing high strain torsional springs cast from elastomeric materials to provide the necessary compliance. The requirements for energy storage capacity with high torsional stiffness and large strain, $75 Nm/rad$ at $0.7 rad$ for the knee, as well as a desire for low mass, low profile compliant elements precluded the use of conventional torsional springs. I participated in design and manufacturing efforts which yielded our first prototype springs.

5.2.2 Type II Leg

The basic design of our robot's leg differs from that of most so-called "hopping robots." The leg, which was constructed prior to my involvement with the project is what we term a *Type I* leg. Figure 5.8 shows the distinction between our Type I leg and the more common *Type II* design. The type I leg has fewer moving parts since it lacks a separate upper leg guide tube. This eliminates one sliding joint which can be a source of practical difficulties relating to alignment and sliding friction. However, the Type I leg includes a hardstop on the overall leg length whereas in the Type II leg, the hardstop acts on the spring length only.

In order to understand how these differences in design affect the vertical hopping motion, we must first consider what occurs during stance. During the first part of the stance phase, the lower leg compresses the leg spring storing the kinetic energy of the robot's vertical motion as elastic energy in the spring. During the second half of the stance phase this energy is returned to the system as the robot begins to move up and eventually lifts off. Unfortunately, this transfer involves a loss energy which translates into a lower lift-off speed (this energy loss is discussed in [27]). Thus the motion of the robot is similar to that of a bouncing ball which decreases in height with each bounce. In order to maintain a steady hopping height additional energy must be added to the system to account for losses. The ball screw shown in the figure compresses the leg spring during the stance phase and adds energy to the system to maintain a stable hopping height.

Now, the hardstop of the Type I leg constrains the overall leg length and prevents the spring from fully extending before lift-off. However, the Type II leg constrains only the spring length and so the spring expands fully returning all the added energy before the robot lifts off. How much elastic energy is lost? Assuming a linear helical coil spring, the elastic energy contained in the leg spring is given by

$$E_{spring} = \frac{1}{2}k_{spring}\Delta^2$$

where k_{spring} is the spring rate and Δ represents the compression of the spring from its free length. If the spring contains a precompression, Δ_{pc}, then the elastic energy lost at lift-off is given by

$$\Delta E_{lo} = \frac{1}{2}k_{spring}(\Delta_{lo}^2 - \Delta_{pc}^2) \tag{5.4}$$

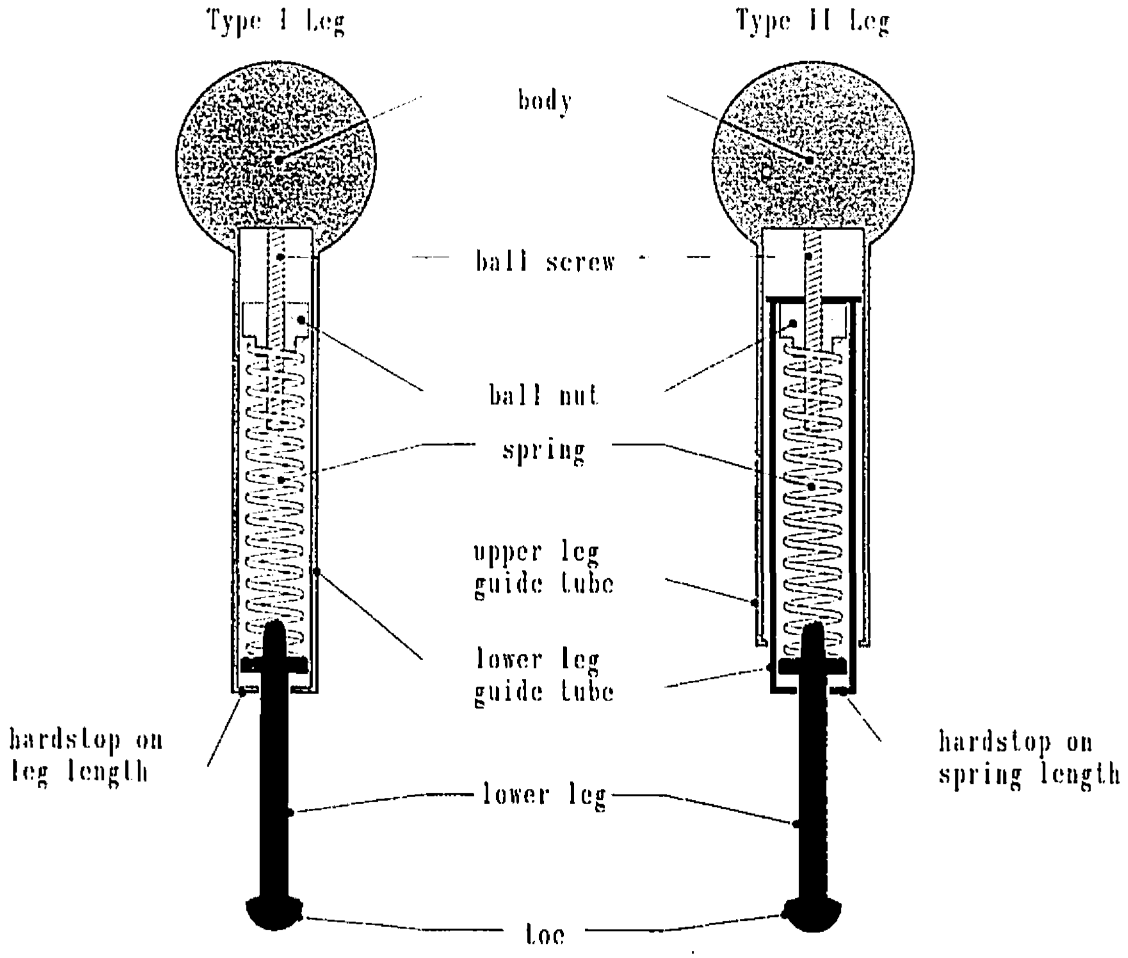

Figure 5.8: *Type II Leg. In a Type I leg the leg length is constrained by a mechanical hardstop (left). At lift-off, the elastic energy stored in the spring by actuator compression is lost since the spring cannot extend to its full length. In a Type II leg (right) The hardstop constrains the spring length not the leg length so the spring is free to extend to its full length before lift-off. Currently the ARL Monopod uses a Type I leg and loses approximately $3.7J/step$ in unrecovered elastic energy accounting for 14% of overall energy cost at zero speed.*

where Δ_{lo} is the compression of the spring at lift-off. In a Type II leg, the spring compression at lift-off is equal to the precompression so equation (5.4) confirms that no energy is lost. In a Type I leg, however, the spring cannot extend fully since the leg length is constrained by a hardstop. Experimental data shows that $\Delta_{lo} = 0.048m$ while $\Delta_{pc} = 0.021m$. Thus for our $4kN/m$ leg spring, the elastic energy lost per step is given by equation (5.4) as $\Delta E_{lo} = 3.7J$ which accounts for 14% of the overall energy cost for hopping at zero running speed(8%@$1.2m/s$).

5.2.3 Hybrid Sensors

Any control algorithm is only as good as the sensor signals it receives as input. As discussed in Section 5.1.1, sensor noise is reflected onto actuator output reducing tracking performance and increasing the energetic cost of control. Currently we are using Hewlett Packard HEDS-6000 series incremental optical encoders for all angular position measurements. These encoders supply a digital quadrature signal and interface easily with the XP/DCS. Moreover, they do not drift and have a constant resolution of about $\frac{1}{12}^{\circ}$ over an infinite range. While these sensors are ideal for motors which experience multiple revolutions ($15bits$ for 6 revolutions), they are less well suited for measuring joint angles with a low range ($10bits$ for 90°). Analog sensors such as potentiometers can have a much better resolution but must be calibrated and are susceptible to electro-magnetic interference.

Since the resolution is limited primarily by noise generated between the potentiometer and the A/D circuitry, it is essential to minimize this distance. To this end, we have developed a hybrid sensor based on an infinite resolution potentiometer coupled with a local analog to digital converter. In this way, the sensor takes advantage of the infinite resolution of the analog device but behaves like a digital device from the point of view of interfacing and insensitivity to electro-magnetic noise. The circuit diagram for this sensor is shown in Figure 5.9. The circuit is based on the MAX187 serial A/D converter chip and features active filtering of the input signal as well as a scalable input range. This feature means that the sensor will give true 12 bit resolution over any selected measuring range up to the potentiometer maximum of 340°. Taking advantage of surface mount technology, the entire device fits on a 27mm diameter circuit board attached directly to the potentiometer.

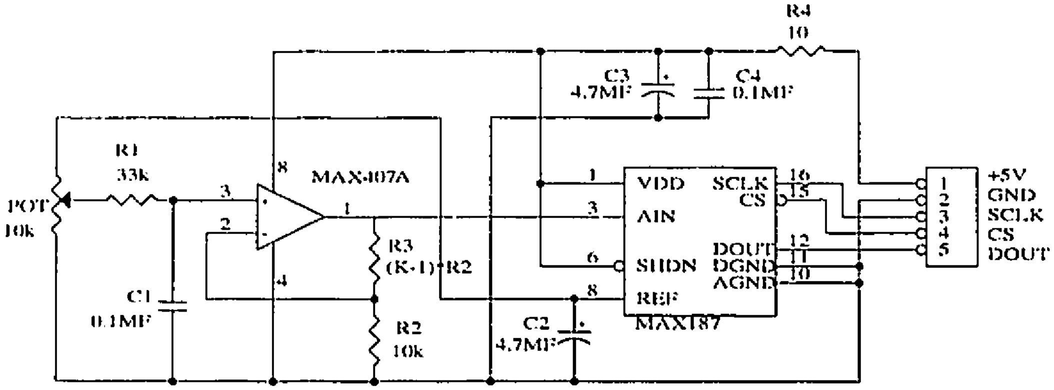

Figure 5.9: *Angle Sensor A/D circuitry*

Preliminary experiments are encouraging especially over small displacements. Figure 5.10 shows experimental results comparing optical encoder to hybrid sensor signals. The upper field clearly shows quantization noise on the encoder signal (upper curve) while the hybrid sensor accurately measures within the A/D converter resolution of $\pm 1 bit$ (lower curve).

The improvement is more pronounced when rate signals are compared. The position signals, q, were differentiated and filtered online in software to obtain rates, $\dot{q}$, through a 1^{st} order IIR filter of the form

$$\dot{q}_n = e^{-\omega_c T}\dot{q}_{n-1} + (1 - e^{-\omega_c T})(q_n - q_{n-1})/T$$

where ω_c is the filter cutoff frequency ($10Hz$) and T is the sampling period ($1ms$). The resulting rates are given in the lower field. The quantization of the encoder signal converts to large slow spikes (upper curve) while the hybrid sensor signal has a much higher signal-to-noise ratio and the noise contains mostly high bandwidth components that are more easily processed (lower curve). The encoder signals have been intentionally offset for clarity and are shown above the hybrid sensor signals.

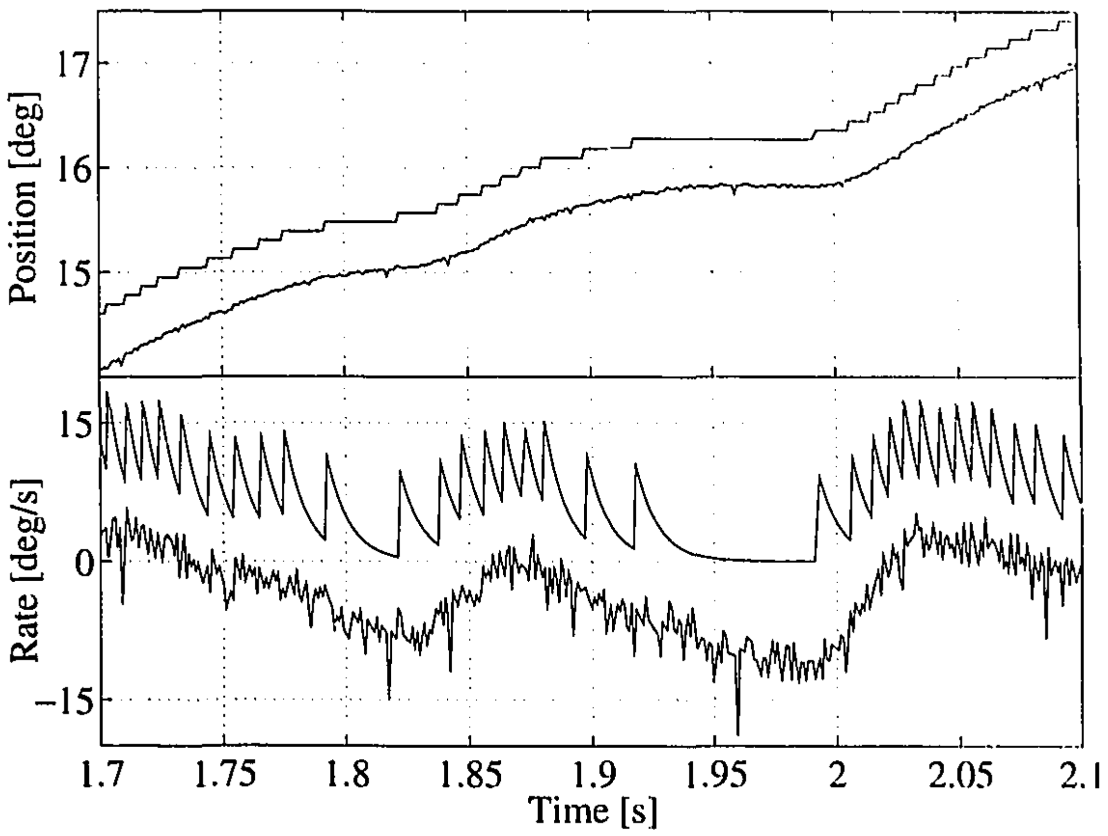

Figure 5.10: *Hybrid Sensor vs. Optical Encoder. For both sensors position signals were differentiated and filtered in software to obtain rate signals. Encoder signals have been shifted for clarity and are shown above Hybrid Sensor signals.*

These hybrid sensors will replace the encoders measuring hip angle and pitch angle. Moreover, CARL, the second generation revolute jointed robot constructed at ARL [18] will use these sensors at 5 locations.

Chapter 6

Conclusion

A project of this type involves many disciplines and affords an excellent opportunity to experience first hand the difficulties and rewards offered by the field of experimental, legged robotics research. Such experimentation when performed on a conceptually simple machine can be a great motivator for developing new ideas since the machine is simple enough to be approachable by analytical methods yet it encompasses all the relevant dynamic properties of active balance and legged locomotion. Far from being an academic exercise, work on this machine has provided a great deal of experience which will doubtless be incorporated into future machines built at ARL. At the same time, our current robot still has much to tell us and there is no lack of ideas which may be tested on the device.

Experiments with our planar, electric monopod have shown that electric actuation for dynamic running robots is feasible despite power limited actuation. We have successfully adapted traditional control algorithms, original designed for much more powerful actuation systems, to operate with $80W$ electric motors. Moreover, a detailed energetic analysis has provided useful insights into how power is used in the running cycle as well as how this power cost may be reduced. Such insights play a key role in the design and control algorithm development of future legged robots at ARL and have already been employed in the design of CARL, our compliant articulated robotic leg.

Even without major efforts towards maximizing performance, our robot has the best energetic performance, as measured by specific resistance, among all powered legged machines. Our experiences with this device give us confidence that a fully-autonomous, electrically-actuated, dynamically-balanced quadruped can be constructed.

Future Work

The experiments performed so far with our conceptually simple robot have taught us a great deal about dynamic locomotion in general. Although any practical device will be much different from our current monopod, there is still much that this machine can teach us. To this end we propose the following, non-exhaustive list of modifications to the physical device and its control algorithms which could deepen our practical understanding of legged locomotion.

The inherent design of the leg currently implemented on the robot accounts for a loss of 14% of all the energy added to vertical motion at zero speed. A new leg based on a *Type II* design discussed in Section 5.2.2 would allow some of this lost elastic energy to be recovered. This would further improve the energetic performance of the machine.

A detailed energetic analysis confirmed that energy output during the flight phase becomes more important as running speed increases. Therefore, efforts towards minimizing energy consumption should concentrate on the flight phase controllers which backdrive the leg actuator and servo the leg angle. The locomotion time variable provides a valuable opportunity for investigating new control strategies. Also controllers which explicitly minimizing energy output of actuators should be investigated. Robust control theory offers techniques which may be applicable to this type of problem.

Finally, the most promising strategy for minimizing energy cost of locomotion involves implementing passive running with a hip compliance in series with the actuator. Passive dynamics is recognized as a key concept for reducing energy consumption in biological systems. Although this type of motion has been investigated for legged machines, no one has yet been able to control the motion in a stable fashion. We have developed at ARL a controller which successfully stabilizes the passive dynamic running motion of a simplified version of our robot. This success should be followed by experimental implementation of these ideas on the physical device.

Bibliography

[1] *XP/DCS CPU/MOD Rev. B Technical Manual.* Evergreen Design, Branford Ct., 1989.

[2] Interelectric AG. *Maxon Motor.* Sachseln, Switzerland, 91/92.

[3] S. Hirose S. Aoki and J. Miyake. Terrain adaptive quadru-track vehicle helios ii. In *Int. Symp. on Industrial Robots*, Tokyo, Japan, Oct 1989.

[4] M. G. Bekker. *Introduction to Terrain-Vehicle Systems.* University of Michigan Press, Ann Arbor, Mich, 1969.

[5] M. Buehler, D. E. Koditschek, and P. J. Kindlmann. Planning and Control of Robotic Juggling and Catching Tasks. *Int. J. Robotics Research*, 13(2):101–118, 1994.

[6] G. A. Cavagna and M. Kaneko. Mechanical work and efficiency in level walking and running. *J. Physiol.*, 268:467–481, 1977.

[7] C. T. Chen. *Linear System Theory and Design.* Holt, Rinehart and Winston, Inc., New York, 1984.

[8] W. Cox. Big muskie. *The Ohio State Engineer*, pages 25–52, Jan 1970.

[9] K. J. Waldron et al. Configuration design of the adaptive suspension vehicle. *Int. J. Robotics Research*, 3(2):37–48, 1984.

[10] G. Gabrielli and T. H. von Karman. What price speed? *Mechanical Engineering*, 72(10):775–781, 1950.

[11] P. Gregorio, M. Ahmadi, and M. Buehler. Experiments with an electrically actuated planar hopping robot. In T. Yoshikawa and F. Miyazaki, editors, *Experimental Robotics III*. Springer-Verlag, 1994.

[12] P. Gregorio and M. Buehler. Specific resistance and legged robots (extended abstract submitted). Int. Conf. on Intelligent Autonomous Systems: IAS-4, Mar 1995.

[13] S. Hirose and Y. Umetani. The basic motion regulation system for a quadruped walking machine. In *Design Engineering Technical Conference, ASME Paper 80-DET-34*, Los Angeles, 1980.

[14] R. Margaria. *Biomechanics and energetics of muscular exercise*. Oxford University Press, 1976.

[15] K. Matsuoka. A mechanical model of repetitive hopping movements. *Biomechanisms*, 5, 1980.

[16] T. McGeer. Passive dynamic walking. *Int. J. Robotics Research*, 9(2), 1990.

[17] T. A. McMahon and G. C. Cheng. The mechanics of running: how does stiffnes couple with speed? *J. Biomechanics*, 23:65–78, 1990.

[18] G. Mennitto, P. Gregoire, and M. Buehler. CARL: A Compliant Articulated Robotic Leg for Dynamic Locomotion. In *Int. Conf. Intelligent Auton. Syst.*, page (to appear), Karlsruhe, Germany, Mar 1995.

[19] H. Miura and I. Shimoyama. Dynamic walk of a biped. *Int. J. Robotics Research*, 3, 1984.

[20] M. M. Moghaddam. A planar virtual motion system for legged robots. M.Eng. Project Report, McGill University, Apr 1993.

[21] R. S. Mosher. Test and evaluation of a versatile walking truck. In *Proceedings of Off-Road Mobility Research Symposium*, pages 359–379, Washington, D.C., 1968. International Society for Terrain Vehicle Systems.

[22] K. V. Papantoniou. Control architecture for an electrical, actively balanced multi-leg robot, based on experiments with a planar one leg machine. In *IFAC*, Vienna, Austria, 1991.

[23] K. V. Papantoniou. Electromechanical design for an electrically powered, actively balanced one leg planar robot. In *Proc. IEEE/RSJ Conf. Intelligent Systems and Robots*, Osaka, Japan, 1991.

[24] K. V. Papantoniou. Experiments concerning the power efficiency during locomotion of an electrical, actively balanced one-leg planar robot. In *Fourth World Conf. on Robotics Research*, Pittsburg, Pennsylvania, Sep 1991. RI/SME.

[25] L. G. C. E. Pugh. The relation of oxygen intake and speed in competetion cycling and comparative observations on the bicycle ergometer. *J.Physiol*, 241:795–808, 1974.

[26] D. R. Pugh, et. al. Technical description of the adaptive suspension vehicle. *Int. J. Robotics Research*, 9(2), Apr 1990.

[27] H. Rad, P. Gregorio, and M. Buehler. Design, modeling and control of a hopping robot. In *Proc. IEEE/RSJ Conf. Intelligent Systems and Robots*, pages 1778–1785, Yokohama, Japan, Jul 1993.

[28] M. H. Raibert. Dynamic stability and resonance in a one-legged hopping machine. *4th Symp. Theory and Practice of Robots and Manipulators*, 1981.

[29] M. H. Raibert. *Legged Robots That Balance*. MIT Press, Cambridge, MA, 1986.

[30] M. H. Raibert. Legged robots. In P. H. Winston and S. A. Shellard, editors, *Artificial Intelligence at MIT*, pages 149–179. MIT Press, Cambridge, MA, 1990.

[31] M. H. Raibert and C. M. Thompson. Passive dynamic running. In V. Hayward and O. Khatib, editors, *Experimental Robotics I*, pages 74 83. Springer-Verlag, NY, 1989.

[32] M. H. Raibert, et al. Dynamically stable legged locomotion. Technical Report 1179 (LL-6), MIT AI Laboratory, 1989.

[33] H. D. Taghirad. Design, analysis and control of a hopping robot. M.Eng. Project Report, McGill University, Apr 1993.